Improving the sensitivity of stop searches with on-shell constrained invariant mass variables

Won Sang Cho,[a,b] **James S. Gainer,**[a] **Doojin Kim,**[a,1] **Konstantin T. Matchev,**[a] **Filip Moortgat,**[c] **Luc Pape**[c] **and Myeonghun Park**[d,e,f]

[a]*Physics Department, University of Florida,*
Gainesville, FL 32611, U.S.A.

[b]*Center for Theoretical Physics of the Universe, Institute for Basic Science (IBS),*
Daejeon 305-811, Korea

[c]*CERN,*
Geneva CH-1211, Switzerland

[d]*Kavli IPMU (WPI), The University of Tokyo,*
Kashiwa, Chiba 277-8583, Japan

[e]*Asia Pacific Center for Theoretical Physics,*
77 Cheongam-Ro, Nam-Gu, Pohang 790-784, Korea

[f]*Department of Physics, Postech,*
Pohang 790-784, Korea

E-mail: hepkosmos@ibs.re.kr, jgainer137@gmail.com, immworry@ufl.edu, matchev@ufl.edu, filip.moortgat@cern.ch, luc.pape@cern.ch, parc@apctp.org

ABSTRACT: The search for light stops is of paramount importance, both in general as a promising path to the discovery of beyond the standard model physics and more specifically as a way of evaluating the success of the naturalness paradigm. While the LHC experiments have ruled out much of the relevant parameter space, there are "stop gaps", i.e., values of sparticle masses for which existing LHC analyses have relatively little sensitivity to light stops. We point out that techniques involving on-shell constrained M_2 variables can do much to enhance sensitivity in this region and hence help close the stop gaps. We demonstrate the use of these variables for several benchmark points and describe the effect of realistic complications, such as detector effects and combinatorial backgrounds, in order to provide a useful toolkit for light stop searches in particular, and new physics searches at the LHC in general.

[1]Corresponding author.

Contents

1 Introduction

Supersymmetry (SUSY) [1] is an important framework for beyond the Standard Model physics, as, among other features, it provides an explanation of the relative lightness of the recently discovered Higgs boson [2, 3] and, potentially, an explanation of dark matter. The search for SUSY at the CERN Large Hadron Collider (LHC), is therefore of considerable importance. The generic SUSY discovery channel is missing transverse energy (MET) accompanied by hard jets, which results from the production of gluinos and/or first

generation squarks via the strong interaction, followed by the subsequent decay of these sparticles to final states that include an undetected lightest SUSY particle (LSP), which is a dark matter candidate. However, the LHC has yet to find evidence of such a signal [4–11], which strongly motivates looking for SUSY elsewhere. Another class of strong production processes, with somewhat lower cross sections, involves the production of third generation squarks: the stop and the sbottom.

1.1 Motivation for stop searches

Stop production has long been recognized as a viable SUSY discovery channel [12–19] and has been looked for at LEP [20–24] and the Tevatron [25–27], as well as at the LHC [7, 9, 28–41]. Searches for the stop are especially well-motivated theoretically because in many models, the stop is expected to be the lightest squark for three principal reasons:

1. The beta function for a squark mass contains a *positive* term proportional to the corresponding Yukawa coupling. The effect of such a positive term is to suppress the mass when evolved from a high energy scale. Since the top Yukawa coupling is the largest Yukawa coupling, one generically expects the stop soft mass parameter to emerge as the lightest of the squark soft masses after RGE evolution from some high energy scale [42]. (At large $\tan\beta$, similar arguments will apply to the sbottom mass as well.)

2. The left-right off-diagonal mixing in the squark mass matrix reduces the smaller mass eigenvalue via level repulsion. The smaller of the two eigenvalues is therefore reduced relative to the corresponding diagonal element. The left-right mixing is an SU(2)-breaking effect, proportional to the Higgs vacuum expectation value and hence to the Yukawa coupling. Thus the stop is, again, the squark that would be most affected by a mass-lowering effect.

3. The radiative corrections to the tree-level relation among m_Z and the Higgs soft mass parameters, which sets the electroweak scale, are dominated by stop loops. Hence a large stop mass would destabilize the hierarchy (this has become known as the little hierarchy problem). The desire to avoid excessive fine-tuning of the electroweak scale has spurred interest in "natural SUSY" models in which the top squark is among the lightest particles in the spectrum [42–46].

Thus in this paper we will consider strategies to discover stops. Although we have in mind searching for the stop in an arbitrary SUSY model, everything we will say applies equally to other BSM models with "top partners".[1] We assume that all other colored sparticles besides the "stop" are either sufficiently heavy to be ignored or nonexistent. We are especially interested in what can be done to extend sensitivity into regions of parameter space where existing LHC searches have not had sufficient sensitivity to discover or rule out the stop. Our approach is complementary to several recent analyses which have targeted similarly difficult parameter space regions for stop discovery [48–79].

---

[1] Our discussion will also apply to situations where there are no new particles and instead the top quark itself undergoes a rare decay involving more than one invisible particle [47].
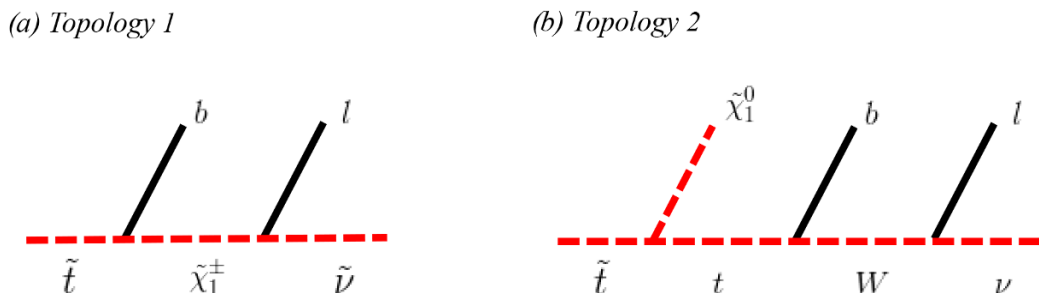
Figure 1. The two signal decay topologies under consideration in this paper. In diagram (a), a stop (antistop) decays to a bottom (antibottom) quark and a positively (negatively) charged on-shell chargino; the chargino decays into an antilepton (lepton) and sneutrino (antisneutrino). In diagram (b), the stop (antistop) decays to a top (antitop) quark and a neutralino. The top (antitop) in turns decays to a bottom (antibottom) quark and a positively (negatively) on-shell charged $W^\pm$ boson, which decays, in turn, to an antilepton (lepton) and neutrino (antineutrino). We refer to the topology in diagram (a) as "Topology 1" and the topology in diagram (b) as "Topology 2".

1.2 Stop decays

Having identified and motivated the production mode that we will consider, we now must decide on the manner in which the particles will decay. Unlike other squarks, for which only the gauge couplings are non-negligible (thereby reducing the number of potentially relevant decay modes), stops have many viable decay modes — there exist two-body decays of stops to gluinos ($\tilde{t} \to \tilde{g} + t$), neutralinos ($\tilde{t} \to \tilde{\chi}_i^0 + t$), charginos ($\tilde{t} \to \tilde{\chi}_i^+ + b$), gravitinos ($\tilde{t} \to \tilde{G} + t$) [18], or even other stops ($\tilde{t}_2 \to \tilde{t}_1 + Z$) [46] and sbottoms ($\tilde{t} \to \tilde{b} + W^+$) [80]. When the two-body decays are suppressed, there are several three-body decays which may dominate, e.g. $\tilde{t} \to bW^+\tilde{\chi}_i^0$, $\tilde{t} \to bW^+\tilde{G}$, $\tilde{t} \to b\ell^+\tilde{\nu}$, $\tilde{t} \to b\nu\tilde{\ell}^+$, etc. [14, 15, 18, 19]. Finally, there can also be loop-induced two-body decays, e.g. $\tilde{t} \to c\tilde{\chi}_i^0$ [14, 15].

In this paper we shall focus on the most challenging scenario, in which the stop produces[2] the same visible particles as a top quark decaying leptonically. In particular, we shall consider the two signal decay topologies shown in figure 1, which commonly occur in realistic models.[3] In the process of figure 1(a), which we refer to as "Topology 1", the stop decay chain is identical to the "leptonic" decay of a top quark; the only differences are that here the role of the $W^\pm$ is played by the chargino $\tilde{\chi}_1^\pm$, and the role of the neutrino is played by the sneutrino $\tilde{\nu}$. (The sneutrino may further decay invisibly to another DM candidate; since the sneutrino is on-shell, this does not affect our analysis.) In the process of figure 1(b), which we shall refer to as "Topology 2", the stop decays to a top quark and a neutralino first; the top then decays leptonically. The resulting *visible* final state is the same, the difference now is that there are *two* invisible particles — a neutralino $\tilde{\chi}_1^0$ and a

---

[2]As usual, we assume that the stop decay proceeds through a "decay chain" of sequential decays of on-shell intermediate particles.

[3]In principle, in addition to the two examples from figure 1, there are many other decay topologies which can mimic a top decay — for example, there can be additional invisible particles emitted in this process [81–84], or the neutralino in figure 1(b) can be emitted in between the bottom quark and the lepton.
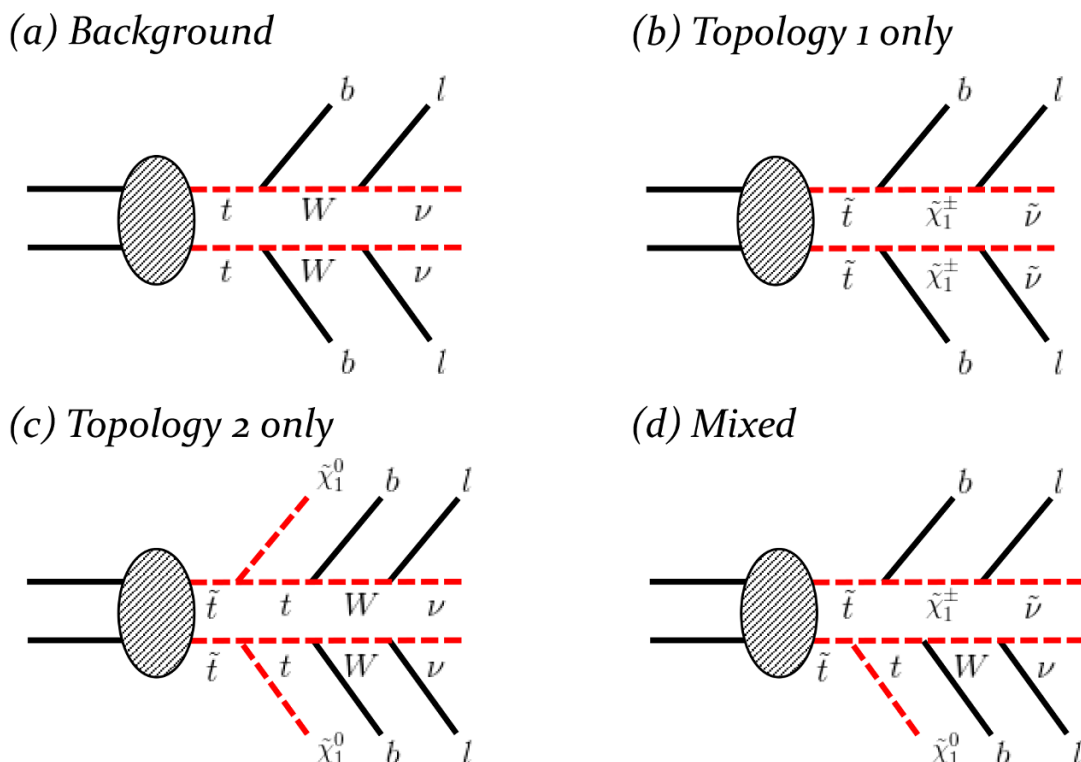
Figure 2. The four event topologies considered in this paper. Diagram (a) gives the background event topology, where the top quarks decay leptonically, i.e., as in figure 1(a), but with the charginos replaced by $W^\pm$ bosons and the sneutrinos replaced by neutrinos. Diagram (b) is the (signal) event topology when both stops decay according to decay Topology 1, diagram (c) is the event topology when both stops decay following Topology 2, and diagram (d) is the mixed event topology when one stop decays according to Topology 1 and the other according to Topology 2.

neutrino ν. When studying Topology 2, we shall assume that the mass splitting between the stop and the neutralino is large enough that the top quark produced in this decay is on-shell, as this makes it *more* difficult to distinguish the signal from top backgrounds.

Specifically, we will consider how to discriminate between stop production, where both stops decay according to one of the topologies in figure 1, and the irreducible background from $t\bar{t}$ dilepton events. Figure 2(a) illustrates the background event topology, while the corresponding three possible signal event topologies are depicted in figures 2(b-d). In all these processes, the observed final state consists of two b-jets, two opposite sign (OS) leptons, and MET, which makes it quite challenging to discover stops in this channel.

Note in particular that our analysis will allow for the mixed event topology of figure 2(d). This is because we shall *not* make any assumptions about the relative branching fraction between Topologies 1 and 2 in figure 1. If the two branching fractions are comparable, there is a sizable fraction of events of the type depicted in figure 2(d); their number benefits also from the combinatorial factor of 2 relative to the events in figure 2(b) or the events in figure 2(c).
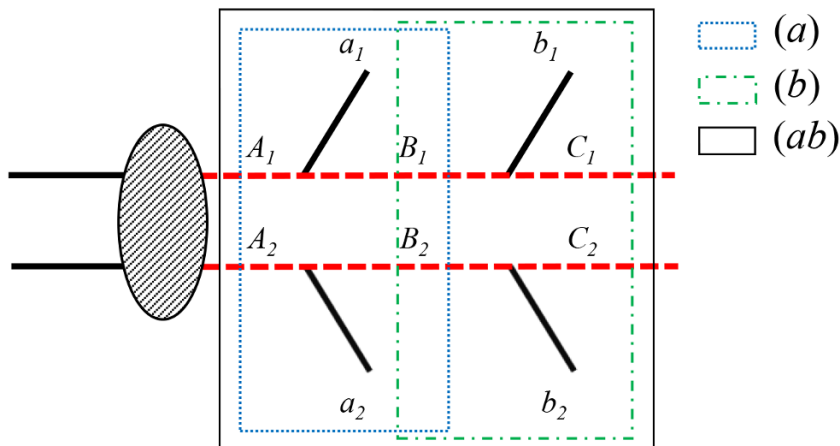
Figure 3. The background event topology of figure 2(a) with the corresponding subsystems explicitly delineated. The blue dotted, green dot-dashed, and black solid lines indicate the subsystems (a), (b), and (ab), respectively. See also table 1.

1.3 On-shell constrained M_2 variables

In this paper we investigate the benefit of the recently proposed on-shell constrained M_2 variables [85–87] in discriminating between the signal events of figure 2(b-d) and the main background shown in figure 2(a). The M_2 variables are the natural $3 + 1$-dimensional generalizations [85] of the Cambridge M_{T2} variable [88, 89], which is already known as a useful tool for background suppression [90–92]. Both M_2 and M_{T2} were designed for events in which particles are pair produced and decay semi-invisibly. (I.e., some of the decay products are invisible.) The variables can then be computed for different subsystems in the event, or for the original event as a whole [93]. For example, in the case of the background $t\bar{t}$ events from figure 2(a), there are three possibilities, which are shown in figure 3. We shall follow the notation of [87] and label these three possibilities as (ab), (a), and (b).

In the spirit of many other kinematic variables such as M_{T2} [88], M_{2C} [94], and M_{CT2} [95], the M_2 variables are obtained by minimizing some parent invariant mass with respect to the momenta of the invisible daughter particles. (The exact definition and basic properties of the constrained M_2 variables are reviewed in section 2 below.) In the process of minimization, one may additionally impose certain kinematic constraints which follow from the hypothesized event topology. The main advantage of the M_2 class of variables is that, being $3 + 1$-dimensional, they allow one to incorporate all known kinematic constraints [86, 87]. For example, M_{T2} and M_{CT2} are transverse variables, and the only constraint which can be used in their calculation is the MET constraint. On the other hand, in calculating an M_2 variable, one is free to impose additional mass shell conditions following either from a previous measurement (as in the case of M_{2C}) or from a theoretical hypothesis about the specific nature of the events, e.g. that the two decay chains in figure 3 are the same and thus $M_{A_1} = M_{A_2}$, $M_{B_1} = M_{B_2}$ and $M_{C_1} = M_{C_2}$.

The presence of additional on-shell constraints will generally increase the calculated value of M_2 — the more constraints there are, the larger the value of M_2. This simple

observation will be at the center of our discussion below, and we shall use it in several different ways:

- The imposition of the additional constraints raises the value of M_2, distorting the shape of the M_2 distribution by increasing the populations of the higher M_2 bins. We can use this effect to increase the signal efficiency in those cases where the background M_2 distribution is bounded by an upper kinematic endpoint, while the signal M_2 distribution extends beyond this kinematic endpoint. This effect will be discussed and illustrated in section 3 for signal events with Topology 1 only, and in section 4 for signal events with Topology 2 only. In either case, the two top squarks decay identically, giving rise to the "symmetric" event topologies of figure 2(b) and figure 2(c), respectively.

- The kinematic variables M_{T2} and M_2 were originally designed for symmetric events, and intended to be used for such events only. But what if the actual event is "asymmetric" and the two parent particles decay in a different manner, e.g., as in figure 2(d)? There are two possible approaches. First, one could suitably modify the definition of M_{T2} in order to adapt it to an asymmetric case [96, 97]. This would still work, provided that *both* the signal and background have the same asymmetric event topology. However, what if the background events are symmetric (as in figure 2(a)), while the signal events are asymmetric (as in figure 2(d)) or vice versa? This case is the subject of section 5, in which we shall advocate the use of the conventional "symmetric" on-shell constrained M_2 variables for this asymmetric case as well. As an illustration, we shall consider a particularly difficult scenario, when the kinematic endpoints of the symmetric events with Topology 1 (figure 2(b)) or Topology 2 (figure 2(c)) are too low and are both "buried" inside the background distribution. Nevertheless, when we compute the M_2 variables for the mixed event topology of figure 2(d), we shall find that the signal distribution does extend beyond the background endpoint. The reason for this apparent "endpoint violation" is simply the fact that when calculating M_2, we are applying the "wrong" constraints on the signal events, but the "correct" constraints on the background events.

- The benefit of the on-shell constrained M_2 variables is not limited only to events in which the background M_2 endpoint is violated. We can achieve additional separation of signal from background by studying the size of the shift caused by the application of the on-shell constraints. In section 6 we shall find that this shift is generally larger for signal events with the mixed event topology of figure 2(d) when compared to the corresponding shift for background events. This observation is valid even for signal events which do not violate the background M_2 endpoint. The study presented in section 6 also includes the effects of detector resolution and combinatorial backgrounds.

1.4 Précis

In this paper we put forth four ideas for stop discovery.

1. We propose to use the on-shell constrained M_2 variables from *each* of the three subsystems ((a), (b), and (ab)) [72, 93]. Previous efforts described in the literature have relied mostly on the dileptonic M_{T2} [57, 64, 70, 98].

2. We advocate the use of the on-shell constrained $(3+1)$-dimensional M_2 variables in place of their transverse cousin M_{T2}, due to their ability to "push" more signal events beyond the background endpoints, thus increasing the signal efficiency.[4]

3. We also propose to use the *difference* between the on-shell constrained M_2 variable and its analogue M_{T2} as an additional discriminator against the background.

4. We show that the on-shell constrained M_2 variable is able to specifically target the mixed signal event topology of figure 2(d) and salvage a certain fraction of signal events in difficult scenarios when more conventional cuts would fail.

2 Review of on-shell constrained M_2 variables

In this section we provide a brief review of on-shell constrained M_2 variables. Readers who are familiar with the terminology and notation of ref. [87] may skip directly to section 3. We begin by reminding the reader that there exists a broad class of kinematic variables that are useful in the analysis of events with missing energy. These variables are defined in two steps [85]:

- One first assumes a particular event topology consistent with the final state particles observed in the event.

- One then minimizes an invariant mass quantity in the hypothesized topology over the unknown invisible momenta, subject to certain kinematic constraints.

The best known example of such a variable is the usual transverse mass M_T, [99, 100], which applies to the simple case of one decay chain with a single invisible particle. Although a transverse quantity, M_T can be thought of as the minimum value of the 3+1 dimensional invariant mass, consistent with the measured missing transverse momentum [85]. This example is rather trivial in the sense that imposing the vector constraint of transverse momentum conservation already fixes the (transverse) components of the invisible particle momentum, and there is only one minimization left to do. A much more interesting case arises when there are two decay chains, with one invisible particle in each. Then the concept of M_T is generalized to the stransverse mass, M_{T2} [88], in which one finds the minimum, with respect to the momenta of invisible particles, of the maximum transverse mass of a given particle on either side of a (symmetric) decay topology, again subject to the constraint of total transverse momentum conservation.

---

[4]The variable M_{T2}^W introduced in [56] is a concrete realization of an on-shell constrained M_2 variable in the case when one of the leptons in figure 2 is lost.

Subsystem	Parents	Daughters	Relatives
S	P_i	D_i	R_i
(ab)	$\{A_i\} = \{t, \bar{t}\}$	$\{C_i\} = \{\nu, \bar{\nu}\}$	$\{B_i\} = \{W^+, W^-\}$
(a)	$\{A_i\} = \{t, \bar{t}\}$	$\{B_i\} = \{W^+, W^-\}$	$\{C_i\} = \{\nu, \bar{\nu}\}$
(b)	$\{B_i\} = \{W^+, W^-\}$	$\{C_i\} = \{\nu, \bar{\nu}\}$	$\{A_i\} = \{t, \bar{t}\}$

Table 1. The roles played by different particles in the background process of $t\bar{t}$ production (figure 2(a)), for each of the three subsystems defined in figure 3.

The on-shell constrained M_2 variables described in [87] are analogous to M_{T2}, with two main differences. First, the quantity being minimized is the four-dimensional invariant mass rather than the transverse mass (see also [85, 86, 94]). Second, in addition to transverse momentum conservation, one is free to apply additional on-shell constraints which follow from the assumed event topology. For concreteness, let us use the event topology of figure 3 to illustrate the procedure of defining the different types of M_2 variables, denoted as

$$M_{2\sqcup\sqcup}(S; \tilde{m}). \tag{2.1}$$

Here $S \in \{(ab), (a), (b)\}$ denotes the subsystem under consideration, while $\sqcup$ is an index placeholder to be defined shortly. According to the nomenclature of [87], depending on the subsystem being considered, the intermediate particles A_i, B_i, and C_i fall into one of the following three categories (see table 1):

- *Daughters D_i.* These are the invisible particles at the end of the decay chains in the subsystem under consideration. Following [87], we shall denote their 3-momenta by $\vec{q}_1$ and $\vec{q}_2$, respectively. The value of the M_2 variable (2.1) will be obtained by minimizing over all possible values of $\vec{q}_1$ and $\vec{q}_2$, consistent with the applied kinematic constraints. As usual, we shall take the daughters' masses to be equal:

$$M_{D_1} = M_{D_2} \equiv \tilde{m} \tag{2.2}$$

and denote them with $\tilde{m}$, which will be an input parameter for the M_2 calculation.

- *Parents P_i.* These are the two particles at the top of the decay chains in the subsystem, and their masses will be subject to minimization over the invisible momenta in order to obtain the variable (2.1). When performing this minimization, in addition to the missing transverse momentum constraint

$$\vec{q}_{1T} + \vec{q}_{2T} = \vec{\not{P}}_T, \tag{2.3}$$

we can additionally require that the two parent masses (when considered as functions of the invisible momenta) are the same:

$$M_{P_1}^2(\vec{q}_1, \tilde{m}) = M_{P_2}^2(\vec{q}_2, \tilde{m}). \tag{2.4}$$

The presence (or absence) of this constraint is indicated by the first $\sqcup$ index in (2.1), which takes value C if the constraint is applied, and X otherwise:

$$M_{2C\sqcup}(S; \tilde{m}) \equiv \min_{\substack{\vec{q}_1, \vec{q}_2 \\ \vec{q}_{1T} + \vec{q}_{2T} = \vec{\not{p}}_T \\ M_{P_1}^2(\vec{q}_1, \tilde{m}) = M_{P_2}^2(\vec{q}_2, \tilde{m})}} \{M_{P_1}(\vec{q}_1, \tilde{m})\}, \tag{2.5}$$

$$M_{2X\sqcup}(S; \tilde{m}) \equiv \min_{\substack{\vec{q}_1, \vec{q}_2 \\ \vec{q}_{1T} + \vec{q}_{2T} = \vec{\not{p}}_T}} \{\max[M_{P_1}(\vec{q}_1, \tilde{m}), M_{P_2}(\vec{q}_2, \tilde{m})]\}. \tag{2.6}$$

- *Relatives R_i.* As shown in table 1, the relatives are the remaining particles in the event topology — they are neither parents nor daughters. Depending on the subsystem, relatives can appear either inside or outside the subsystem. Their masses can also be written as functions of the respective daughters' momenta, so by requiring equal masses[5] for the relative particles,

$$M_{R_1}^2(\vec{q}_1, \tilde{m}) = M_{R_2}^2(\vec{q}_2, \tilde{m}), \tag{2.7}$$

we are, in effect, imposing an additional constraint on the minimization over the invisible momenta $\vec{q}_i$. The applicability of the constraint (2.7) will be indicated by the second $\sqcup$ index in (2.1): as before, it will be equal to C if the constraint (2.7) is applied and X otherwise. Altogether, therefore, we have four possible M_2 variables:

$$M_{2CC}(S; \tilde{m}) \equiv \min_{\substack{\vec{q}_1, \vec{q}_2 \\ \vec{q}_{1T} + \vec{q}_{2T} = \vec{\not{p}}_T \\ M_{P_1}^2(\vec{q}_1, \tilde{m}) = M_{P_2}^2(\vec{q}_2, \tilde{m}) \\ M_{R_1}^2(\vec{q}_1, \tilde{m}) = M_{R_2}^2(\vec{q}_2, \tilde{m})}} \{M_{P_1}(\vec{q}_1, \tilde{m})\}, \tag{2.8}$$

$$M_{2CX}(S; \tilde{m}) \equiv \min_{\substack{\vec{q}_1, \vec{q}_2 \\ \vec{q}_{1T} + \vec{q}_{2T} = \vec{\not{p}}_T \\ M_{P_1}^2(\vec{q}_1, \tilde{m}) = M_{P_2}^2(\vec{q}_2, \tilde{m})}} \{M_{P_1}(\vec{q}_1, \tilde{m})\}, \tag{2.9}$$

$$M_{2XC}(S; \tilde{m}) \equiv \min_{\substack{\vec{q}_1, \vec{q}_2 \\ \vec{q}_{1T} + \vec{q}_{2T} = \vec{\not{p}}_T \\ M_{R_1}^2(\vec{q}_1, \tilde{m}) = M_{R_2}^2(\vec{q}_2, \tilde{m})}} \{\max[M_{P_1}(\vec{q}_1, \tilde{m}), M_{P_2}(\vec{q}_2, \tilde{m})]\}, \tag{2.10}$$

$$M_{2XX}(S; \tilde{m}) \equiv \min_{\substack{\vec{q}_1, \vec{q}_2 \\ \vec{q}_{1T} + \vec{q}_{2T} = \vec{\not{p}}_T}} \{\max[M_{P_1}(\vec{q}_1, \tilde{m}), M_{P_2}(\vec{q}_2, \tilde{m})]\}. \tag{2.11}$$

The definitions (2.8)–(2.11) should be contrasted to the analogous definition of the Cambridge M_{T2} variable

$$M_{T2}(S; \tilde{m}) \equiv \min_{\substack{\vec{q}_{1T}, \vec{q}_{2T} \\ \vec{q}_{1T} + \vec{q}_{2T} = \vec{\not{p}}_T}} \{\max[M_{TP_1}(\vec{q}_{1T}, \tilde{m}), M_{TP_2}(\vec{q}_{2T}, \tilde{m})]\}, \tag{2.12}$$

where only the transverse components $\vec{q}_{iT}$ are used, and the objective function (the function that is minimized) is the larger of the two *transverse* masses of the parents.

---

[5]We note that while a parent mass squared is always positive, the mass squared of a *relative* could be negative: keep in mind that the values for the invisible momenta $\vec{q}_1$ and $\vec{q}_2$ found in the minimization process are not the true momenta and could be unphysical, i.e., there is no guarantee that $M_{R_i}^2 > 0$. While one has the option of adding the further constraint that the squared masses of the relative particles be positive, we will not do so in this work.

The main goal of this paper is to investigate and contrast the ability of the variables (2.8)–(2.12) to discriminate between the $t\bar{t}$ background of figure 2(a) and the three types of stop signal events of figure 2(b-d). We shall consider the respective variables for all three subsystems of figure 3. Since we know the mass spectrum for the background event topology, we shall choose the test mass $\tilde{m}$ to be equal to the correct, SM value for the respective daughter particle. In particular,

- In subsystem (ab), the parent particle is the top quark; the daughter particle is the neutrino, whose mass is taken to vanish ($\tilde{m} = 0$). The other, "relative", particle is the $W^{\pm}$ boson. Then *for background events*, all 5 variables (2.8)–(2.12) are bounded from above by the top mass:

$$M_{T2}(ab;0), M_{2XX}(ab;0), M_{2CX}(ab;0), M_{2XC}(ab;0), M_{2CC}(ab;0) \leq m_t, \quad (2.13)$$

  while for signal events, this bound can be violated.

- In subsystem (a), the parent particle is again the top quark. The daughter particle is now the $W^{\pm}$ boson, with mass $\tilde{m} = m_W$. The relative particles are the two neutrinos, which in this case appear downstream outside the subsystem. For background events, the variables are again bounded by the top mass

$$M_{T2}(a;m_W), M_{2XX}(a;m_W), M_{2CX}(a;m_W), M_{2XC}(a;m_W), M_{2CC}(a;m_W) \leq m_t. \quad (2.14)$$

- In subsystem (b) the parent particles are the $W^{\pm}$ bosons, the daughter particles are the two neutrinos with mass $\tilde{m} = 0$, and the relative particles are the top quarks appearing upstream outside the subsystem. The background events obey

$$M_{T2}(b;0), M_{2XX}(b;0), M_{2CX}(b;0), M_{2XC}(b;0), M_{2CC}(b;0) \leq m_W. \quad (2.15)$$

In principle, *each* of the bounds (2.13)–(2.15) allows us to cut 100% of the $t\bar{t}$ background events by removing events with values of the respective subsystem M_2 or M_{T2} variable below the appropriate threshold ("high pass cut"). Therefore, as far as just the background is concerned, we have 15 alternative choices[6] for reducing it, and they should perform comparably well. The differences between the five variables (2.8)–(2.12) begin to emerge when we consider the effect of such a high pass cut on signal events. It has been shown [87] that the variables (2.8)–(2.12) obey the following hierarchy

$$M_{T2}(S;\tilde{m}) = M_{2XX}(S;\tilde{m}) = M_{2CX}(S;\tilde{m}) \leq M_{2XC}(S;\tilde{m}) \leq M_{2CC}(S;\tilde{m}) \quad (2.16)$$

for any subsystem S and any value of $\tilde{m}$. We should therefore expect the distributions of M_{2XC} and M_{2CC} to be more populated at higher values and in particular near their endpoints. As a result, signal events are more likely to pass if the cut is applied on the additionally constrained variables, M_{2XC} and M_{2CC}, as opposed to the less constrained variables M_{T2}, M_{2XX}, and M_{2CX}. This expectation is borne out by the explicit studies below. The property (2.16) offers an opportunity to increase the sensitivity of the LHC experiments to the presence of stop signals of the type described in figure 2(b-d).

---

[6]Each of the five variables (2.8)–(2.12) can be applied for each of the three subsystems (ab), (a), and (b). The explicit definitions of the resulting 15 variables can be found in appendix A.

3 M_2 endpoint study for topology 1

We begin by studying the effectiveness of the on-shell constrained subsystem M_2 variables in the case where both stops in the signal event decay according to Topology 1. This yields the event topology pictured in figure 2(b). The background, as always in this paper, consists of dileptonic top production and is shown in figure 2(a). We remind the reader that when applied to *background events*, all of the on-shell constrained subsystem M_2 variables (as well as M_{T2}) exhibit very well-defined kinematic endpoints given by eqs. (2.13)–(2.15). Therefore, the effectiveness of the M_2 variables in identifying signal events is determined by how many signal events violate the bounds (2.13)–(2.15).

The signal events considered in this section (those of figure 2(b)) have exactly the same topology as the background. Therefore, when applied to *signal events*, the M_2 variables will have well-defined upper kinematic endpoints as well. The precise value of those endpoints will depend on the underlying signal mass spectrum, i.e., on the true values of the stop mass $m_{\tilde{t}}$, the chargino mass $m_{\tilde{\chi}^\pm}$, and the sneutrino mass $m_{\tilde{\nu}}$. For any given point $\{m_{\tilde{t}}, m_{\tilde{\chi}^\pm}, m_{\tilde{\nu}}\}$ in the mass parameter space, using the formulas given in ref. [93], one can compute the expected M_2 kinematic endpoints for the signal, in each of the three subsystems (ab), (a), and (b).[7] Depending on the SUSY mass spectrum, some, all, or none of these signal endpoints will exceed the corresponding background endpoints. In the second half of this section, we shall illustrate each of these three scenarios with specific study points. But first we shall analyze the relevant mass parameter space and categorize the different regions, which are defined by the location of the signal endpoints relative to the background endpoints. This will be the subject of the next subsection.

3.1   Anatomy of the mass parameter space for Topology 1

In order to divide the stop-chargino-sneutrino mass parameter space into regions, we start with the analytical expressions for the M_{T2} signal endpoints [93, 101, 102]. (The endpoints for the corresponding $M_{2\sqcup\sqcup}$ variables are given by the exact same expressions [87].)

$$M_{T2}^{\max}(ab; \tilde{m} = 0) = \frac{m_{\tilde{t}}^2 - m_{\tilde{\nu}}^2}{m_{\tilde{t}}}, \tag{3.1}$$

$$M_{T2}^{\max}(a; \tilde{m} = m_W) = \frac{m_{\tilde{t}}^2 - m_{\tilde{\chi}^\pm}^2}{2m_{\tilde{t}}} + \sqrt{\left(\frac{m_{\tilde{t}}^2 - m_{\tilde{\chi}^\pm}^2}{2m_{\tilde{t}}}\right)^2 + m_W^2}, \tag{3.2}$$

$$M_{T2}^{\max}(b; \tilde{m} = 0) = \sqrt{\frac{\left(m_{\tilde{t}}^2 - m_{\tilde{\nu}}^2\right)\left(m_{\tilde{\chi}^\pm}^2 - m_{\tilde{\nu}}^2\right)}{m_{\tilde{t}}^2}}. \tag{3.3}$$

Now combining, e.g., eqs. (2.13) and (3.1), we find that for the variables in the (ab) subsystem, the signal endpoints exceed the background endpoints if

$$\frac{m_{\tilde{t}}^2 - m_{\tilde{\nu}}^2}{m_{\tilde{t}}} > m_t. \tag{3.4}$$

---

[7]We remind the reader that in this work, the M_2 variables are always computed with test masses corresponding to the background hypothesis; see appendix A.
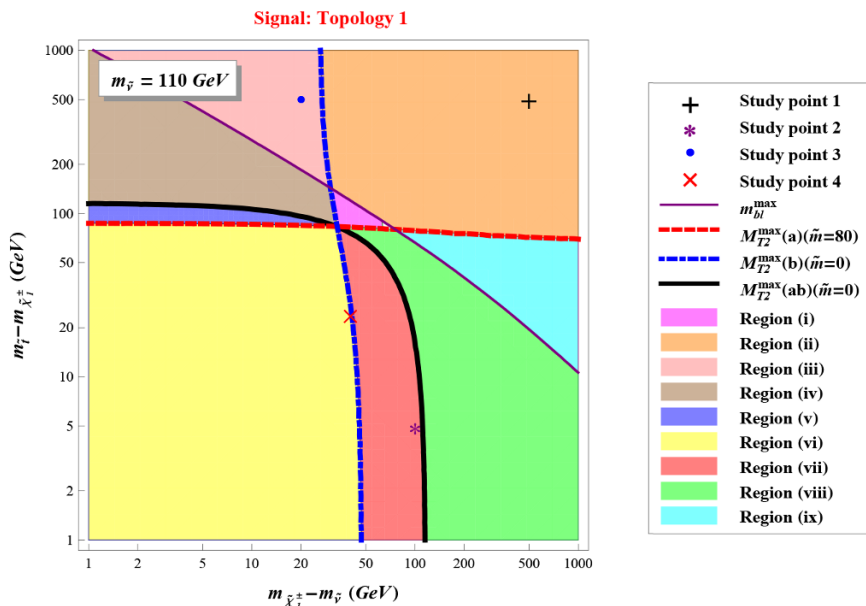
Figure 4. The division of stop-chargino-sneutrino mass parameter space into regions, which are defined by which of the background endpoints are violated by signal events in which both stops decay according to Topology 1. The sneutrino mass has been set to 110 GeV. The four study points considered later in this section are also indicated.

The corresponding region is delineated by the solid black line in figure 4, which shows a slice through the 3-dimensional mass parameter space for fixed $m_{\tilde{\nu}} = 110 \, \text{GeV}$. For convenience we choose to represent the remaining two degrees of freedom as the mass differences $m_{\tilde{\chi}^{\pm}} - m_{\tilde{\nu}}$ and $m_{\tilde{t}} - m_{\tilde{\chi}^{\pm}}$. The region satisfying the condition (3.4) is above and to the right of the solid black line in figure 4. If the SUSY mass spectrum happens to be in this region, the mass splitting between the stop and the sneutrino is sufficiently large to cause some number of signal events to "leak" beyond the background endpoint (2.13). This means that the subsystem (ab) variables are promising variables to cut on in order to separate signal from background.

We can apply similar reasoning to the invariant mass variables in subsystems (a) and (b). For example, comparing eqs. (2.14) and (3.2), we find that the bound (2.14) applicable to background events will be violated if the mass spectrum is such that

$$\frac{m_{\tilde{t}}^2 - m_{\tilde{\chi}^{\pm}}^2}{m_{\tilde{t}}} > \frac{m_t^2 - m_W^2}{m_t}. \tag{3.5}$$

The corresponding region extends above the red dashed line in figure 4. Finally, the condition for violating the background endpoints in subsystem (b) follows from eqs. (2.15) and (3.3):

$$\frac{\left(m_{\tilde{t}}^2 - m_{\tilde{\nu}}^2\right)\left(m_{\tilde{\chi}^{\pm}}^2 - m_{\tilde{\nu}}^2\right)}{m_{\tilde{t}}^2} > m_W^2. \tag{3.6}$$

Region	$m_{b\ell}$ endpoint violation	$M_{T2}(ab)$ endpoint violation	$M_{T2}(a)$ endpoint violation	$M_{T2}(b)$ endpoint violation
i	No	Yes	Yes	Yes
ii	Yes	Yes	Yes	Yes
iii	Yes	Yes	Yes	No
iv	No	Yes	Yes	No
v	No	No	Yes	No
vi	No	No	No	No
vii	No	No	No	Yes
viii	No	Yes	No	Yes
ix	Yes	Yes	No	Yes

Table 2. The regions of stop-chargino-sneutrino mass space, as depicted in figure 4. The four columns describe whether in the given region, the specified background endpoint can be violated by signal events where both stops decay according to Topology 1.

The region where this condition is satisfied is located to the right of the blue dot-dashed line in figure 4.

For completeness, we shall also consider the variable m_{bl}, the invariant mass of the lepton and b quark from a given branch of the decay. The endpoint of this quantity for signal events is given by

$$m_{b\ell}^{\max} = \sqrt{\frac{\left(m_{\tilde{t}}^2 - m_{\tilde{\chi}^\pm}^2\right)\left(m_{\tilde{\chi}^\pm}^2 - m_{\tilde{\nu}}^2\right)}{m_{\tilde{\chi}^\pm}^2}}, \tag{3.7}$$

while background events will obey the bound

$$m_{b\ell} \leq \sqrt{m_t^2 - M_W^2}. \tag{3.8}$$

Therefore the condition for violating the background $m_{b\ell}$ endpoint is

$$\frac{\left(m_{\tilde{t}}^2 - m_{\tilde{\chi}^\pm}^2\right)\left(m_{\tilde{\chi}^\pm}^2 - m_{\tilde{\nu}}^2\right)}{m_{\tilde{\chi}^\pm}^2} > m_t^2 - M_W^2. \tag{3.9}$$

The corresponding region is found above and to the right of the diagonal magenta thin solid line in figure 4.

The conditions implied by eqs. (3.4)–(3.6) and (3.9) divide the mass parameter space of figure 4 into nine distinct color-coded regions, which are defined in table 2. It is easy to verify analytically that the boundaries of the three regions defined by conditions (3.4)–(3.6), i.e., the red, blue, and black curves in figure 4, cross at a single point. For any given sneutrino mass, $m_{\tilde{\nu}}$, the values of the stop mass, $m_{\tilde{t}}$, and the chargino mass, $m_{\tilde{\chi}^\pm}$, corresponding to the triple crossing point are found from the relations

$$\frac{m_{\tilde{t}}^2 - m_{\tilde{\nu}}^2}{m_{\tilde{t}}} = m_t, \qquad \frac{m_{\tilde{\chi}^\pm}^2 - m_{\tilde{\nu}}^2}{m_{\tilde{t}}} = \frac{m_W^2}{m_t}.$$

Study Point	Stop Mass	Chargino Mass	Sneutrino Mass	Region
1	1110 GeV	610 GeV	110 GeV	ii
2	215 GeV	210 GeV	110 GeV	vii
3	630 GeV	130 GeV	110 GeV	iii
4	174 GeV	150 GeV	110 GeV	vi

Table 3. The stop, chargino, and sneutrino masses for the four study points considered in this section, as well as the region of mass parameter space from figure 4 that contains each point.

The map in figure 4 serves a dual purpose. First, it singles out the regions which might be easier to discover, as well as the regions which may pose challenges. Second, within each region, it identifies the variables which might be useful in the analysis (see table 2). For example, in region ii, the mass spectrum is sufficiently split, and all four variables exhibit endpoint violations for signal events. This in turn suggests that separating signal from background should be relatively easy, since we can use any of the four types of invariant mass variables in table 2 to suppress the background without much signal loss. To illustrate the expected phenomenology of region ii, in section 3.2 we shall analyze in detail a specific study point from this region. Its mass spectrum is given in table 3 and its exact location on the map of figure 4 is marked with a black cross (+).

In all but one of the remaining regions of figure 4, some of the endpoints are violated while others are not, thus some variables are expected to perform better than others. We pick two representative study points in regions vii and iii and study them in sections 3.3 and 3.4, respectively. In figure 4, these two study points are marked with the magenta asterisk (∗) and the blue circle (•). The corresponding mass spectra are also listed in table 3.

Finally, region vi deserves a special mention, since it represents a particularly challenging scenario. Here none of the four types of invariant mass variables exhibits an endpoint violation, and the signal events are populating the same kinematic region as the background events. Our fourth study point in table 3 (denoted in figure 4 with the red (×) symbol) belongs to this challenging region and is considered in section 3.5.

3.2 Study point 1: split spectrum in region ii

In this section we shall illustrate the properties of region ii in figure 4 with the study point 1 which is marked with the black (+) symbol. As seen in table 3, this study point has a widely split spectrum; both mass differences $m_{\tilde{t}} - m_{\tilde{\chi}^{\pm}}$ and $m_{\tilde{\chi}^{\pm}} - m_{\tilde{\nu}}$ are 500 GeV. One can therefore expect that the signal distributions for our invariant mass variables will extend well beyond the corresponding background distributions. This is confirmed in figure 5, where we plot distributions for signal events (red lines) and background events (blue lines) for $M_{T2}(S; \tilde{m})$ (dashed lines), $M_{2CC}(S; \tilde{m})$ (solid lines), and $m_{b\ell}$. As always in this section, the signal events are assumed to have the symmetric event topology of figure 2(b), i.e., both stops decay according to Topology 1. Figure 5 shows results for all three subsystems: $S = (ab)$ (upper left panel), $S = (a)$ (upper right panel) and $S = (b)$ (lower left panel). In each case, the trial mass $\tilde{m}$ for the respective daughter particle has been set to the correct value for SM events, as explained in more detail in appendix A.
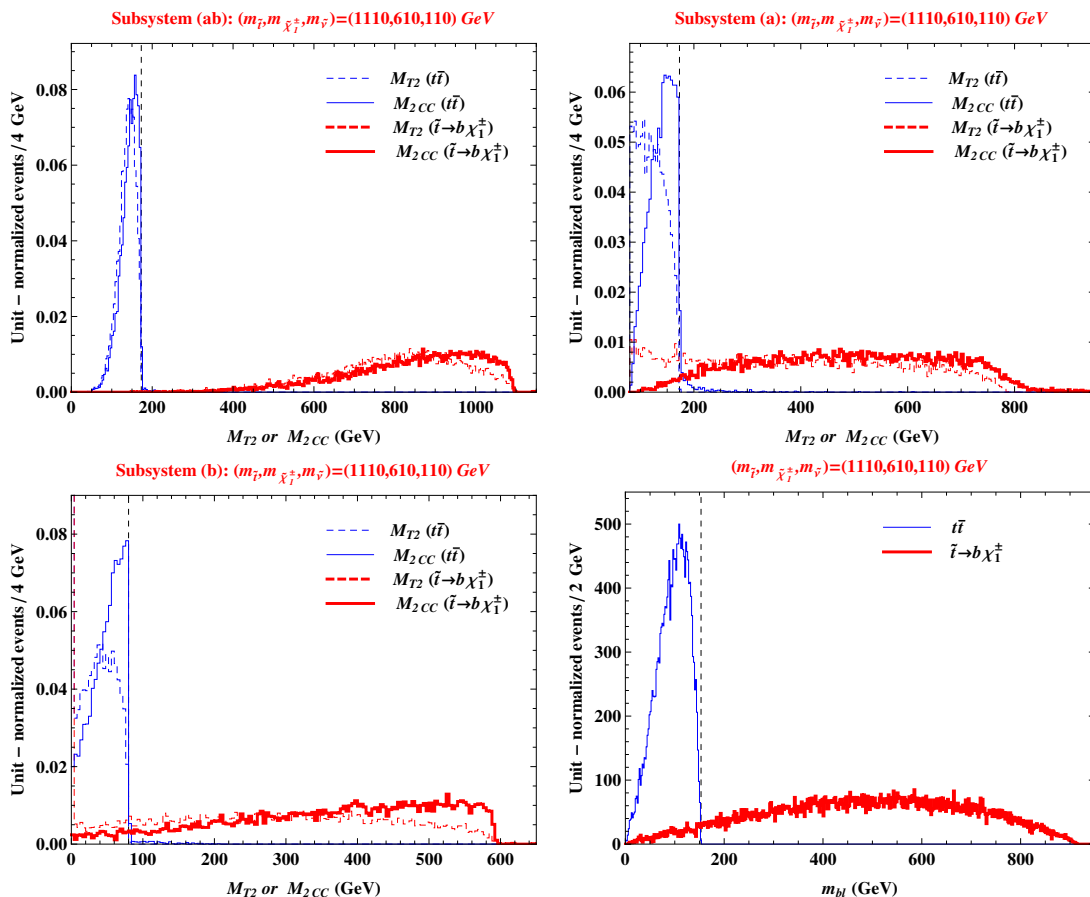
Figure 5. Signal (thick red lines) and background (thin blue lines) distributions for the subsystem variables $M_{T2}(S;\tilde{m})$ (dashed lines) and $M_{2CC}(S;\tilde{m})$ (solid lines). We show results for each of the three possible subsystems: $S = (ab)$ (upper left panel), $S = (a)$ (upper right panel), and $S = (b)$ (lower left panel). The lower right panel shows the analogous distributions for the invariant mass $m_{b\ell}$. The signal events are for study point 1 ($m_{\tilde{t}} = 1110\,\mathrm{GeV}$, $m_{\tilde{\chi}^\pm} = 610\,\mathrm{GeV}$ and $m_{\tilde{\nu}} = 110\,\mathrm{GeV}$) and have the event topology shown in figure 2(b).

In each panel of figure 5, the vertical dashed line marks the location of the kinematic endpoint for background events, as given by eqs. (2.13)–(2.15) and (3.8). As expected, the blue (background) distributions always obey these kinematic endpoints. (The figure has been constructed using parton-level events with no detector modeling or combinatorial backgrounds — these effects will be added later on in section 6.)

On the other hand, the signal events, shown in red, significantly violate the endpoints. In fact, for all four variables considered in figure 5, the vast majority of signal events violate the background endpoints. This is also to be expected, since study point 1 was chosen specifically in region ii, where all four endpoints are expected to be violated (see table 2). This also means that discovery (or exclusion) for this study point should be relatively straightforward.

We have noted above that, on an event by event basis,

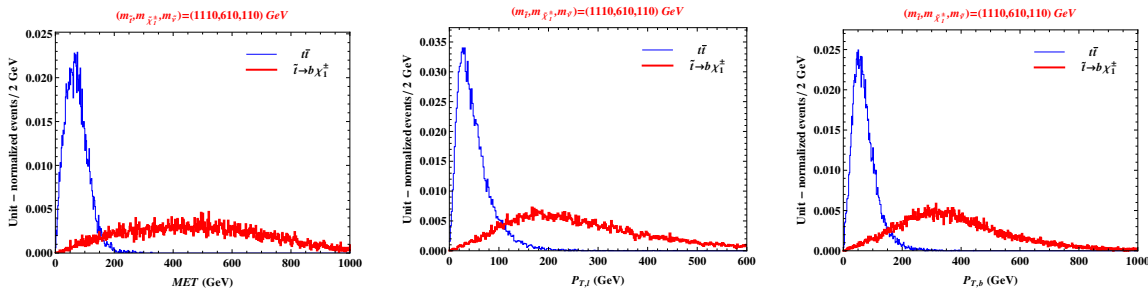$$M_{T2}(S;\tilde{m}) \leq M_{2CC}(s;\tilde{m}). \tag{3.10}$$

Figure 6. Signal (thick red lines) and background (thin blue lines) distributions of some standard variables for study point 1 ($m_{\tilde{t}} = 1110\,\mathrm{GeV}$, $m_{\tilde{\chi}^{\pm}} = 610\,\mathrm{GeV}$ and $m_{\tilde{\nu}} = 110\,\mathrm{GeV}$): the missing transverse energy MET (left panel), the lepton transverse momentum $p_{T,\ell}$ (middle panel), and the b-quark transverse momentum $p_{T,b}$ (right panel).

This is confirmed in figure 5, where the (solid line) M_{2CC} distributions can be seen to be somewhat harder than the respective M_{T2} dashed line distributions. As a result, cutting on M_{2CC} instead of M_{T2} will result in a slightly higher signal efficiency. (The effect is most easily seen for subsystems (a) and (b).)

While the variables shown in figure 5 already allow study point 1 to be discovered or ruled out rather trivially, the same can be accomplished with more conventional variables like the missing transverse energy (MET), the lepton transverse momentum $p_{T,\ell}$, or the b-quark transverse momentum $p_{T,b}$, whose distributions for study point 1 are plotted in figure 6. In all three cases, even though the background distribution does not exhibit a strict endpoint, the signal and background distributions are very well separated, so the signal can be easily isolated. Furthermore, as we can measure four endpoints in figure 5 and there are only three input mass parameters, full mass reconstruction in this case is also possible [93]. In conclusion, the analysis of study point 1 demonstrates that region ii is "easy" in the sense that the experimenter has a plethora of useful tools available for a discovery. It is therefore of interest to consider the other, more challenging, regions of figure 4.

3.3 Study point 2: soft b-jets in region vii

Our second example is in region vii, in which only the variables in subsystem (b) have endpoint violations. The mass spectrum for study point 2 is given in table 3. We notice the relative degeneracy between the stop and chargino masses, which causes the endpoints of the signal $M_{T2}(a)$ and $m_{b\ell}$ distributions to be relatively low. (See eqs. (3.2) and (3.7).) In addition, the sneutrino mass has been chosen so that the signal endpoint (3.1) of the $M_{T2}(ab)$ variable is also below the standard model expectation of (2.13). This leaves the $M_{T2}(b)$ variable as the only viable alternative in region vii.

These observations are illustrated in figure 7 where we plot the relevant invariant mass distributions for study point 2 using the same conventions as in figure 5 above. Again, we assume that all signal events have the event topology shown in figure 2(b), i.e., both stops decay according to Topology 1. Figure 7 confirms that $M_{T2}(b)$ is a good variable to cut on: placing a high pass cut with threshold just above m_t would eliminate all of the background, while leaving almost half of the signal. To determine the optimal value of the threshold and the effectiveness of the cut requires realistic detector simulation (see
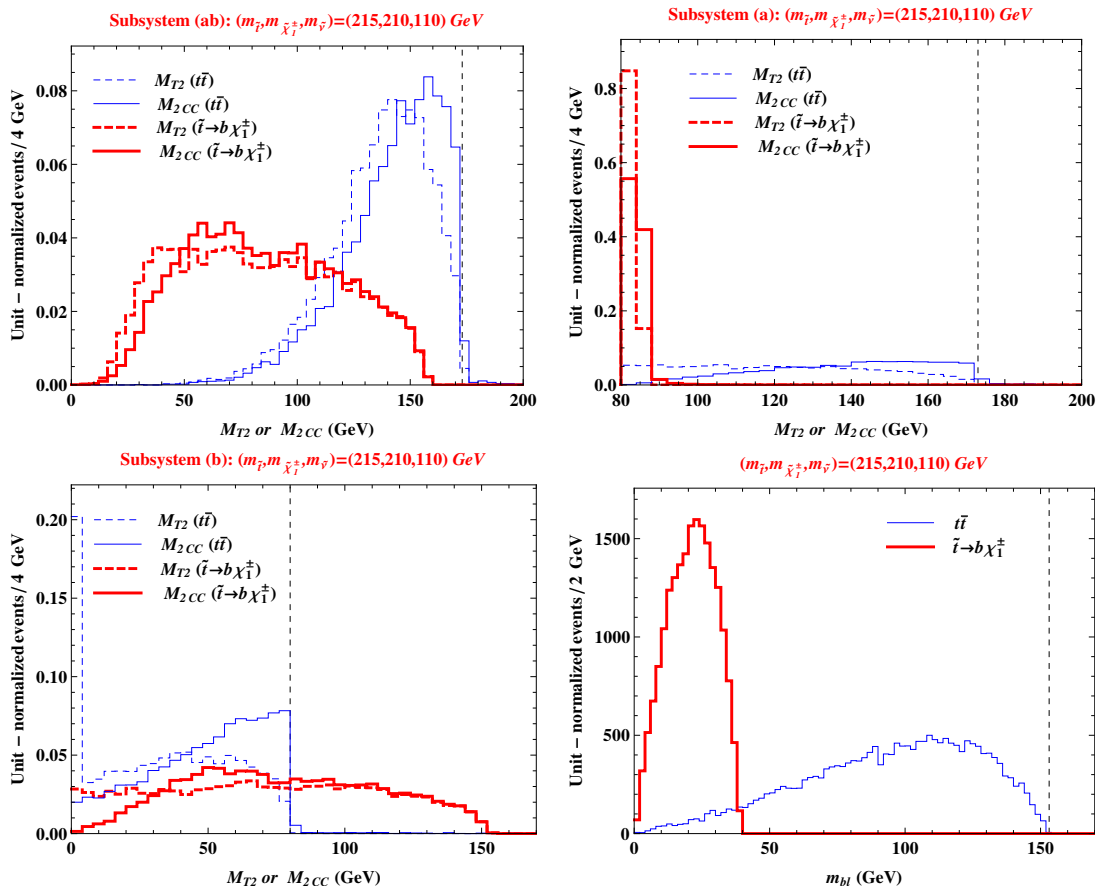
Figure 7. The same as figure 5, but with signal events for study point 2 ($m_{\tilde{t}} = 215\,\mathrm{GeV}$, $m_{\tilde{\chi}^{\pm}} = 210\,\mathrm{GeV}$ and $m_{\tilde{\nu}} = 110\,\mathrm{GeV}$).

section 6), but it is clear that such a cut will often be useful. This observation is not new — the variable $M_{T2}(b)$ has been discussed in the literature under various names, e.g., $M_{T2}^{(210)}$ [93] and dileptonic M_{T2} [57, 64, 70, 98]. Here we would like to contrast $M_{T2}(b)$ to the alternative on-shell constrained variable $M_{2CC}(b)$. The advantage of the latter is the slightly higher signal efficiency. On the other hand, the advantage of the traditional M_{T2} is its simplicity — in its calculation, one does not have to identify the b-jets, thus, one avoids combinatorial ambiguities and the additional penalty due to b-tagging.

Note that the signal and background distributions for the other three variables in figure 7: $M_{T2}(ab)$, $M_{T2}(a)$, and $m_{b\ell}$, also appear to be quite different, so one might wonder whether they could be useful if the cut were inverted (i.e., if one performs a low pass cut). However, we expect other background processes besides $t\bar{t}$ to contribute events at low values and swamp the signal [90–92]. Such backgrounds may not be as well-understood, which is why in this study we shall only consider *high pass* cuts on the invariant mass variables.[8]

---

[8]Additionally we remind the reader that figure 7 (and analogous) figures throughout the work, depict unit normalized distributions for signal and background; in reality the background rates will be far higher than the signal rates in any realistic model. This also makes it more challenging to utilize the differences in shape for a given variable *below* the endpoint; endpoint violation is the preferred feature for discovery.
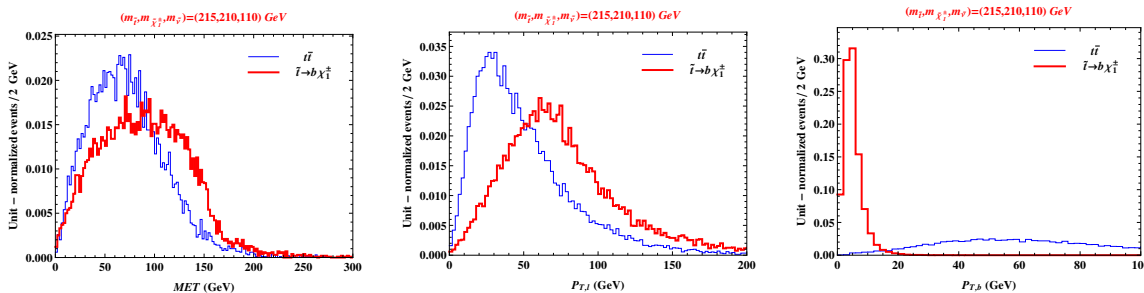
Figure 8. The same as figure 6, but for signal events for study point 2 ($m_{\tilde{t}} = 215\,\text{GeV}$, $m_{\tilde{\chi}^{\pm}} = 210\,\text{GeV}$ and $m_{\tilde{\nu}} = 110\,\text{GeV}$).

Having identified $M_{T2}(b)$ and $M_{2CC}(b)$ as promising variables, one might wonder how the more conventional variables would perform in this case. In figure 8, we show parton-level signal and background distributions for study point 2 for the three more traditional variables considered in figure 6: MET, $p_{T,\ell}$, and $p_{T,b}$. Since the stop-chargino mass splitting is rather small, the b-jets are quite soft and would often not be reconstructed. On the other hand, the MET and $p_{T,\ell}$ distributions show some separation between signal and background, but the separation is less clear than we observed in the case of $M_{T2}(b)$ (the lower left panel of figure 5). Therefore, placing cuts on MET and $p_{T,\ell}$ would not be as effective as cutting on $M_{T2}(b)$.

3.4 Study point 3: soft leptons in region iii

Our next example illustrates the complementarity of the subsystem invariant mass variables. In the previous subsection (3.3), we considered a signal study point with soft b-jets and relatively hard leptons, as seen in figure 8. Now we shall discuss the opposite situation, when the leptons are relatively soft, while the jets are hard. For this purpose, we focus on study point 3 in region iii, where according to table 2 we expect endpoint violations for $M_{T2}(ab)$, $M_{T2}(a)$, and $m_{b\ell}$. This feature is demonstrated in figure 9, where we again compare the signal and background distributions for the same four types of variables as in figures 5 and 7. We see that this time, as expected, the dilepton M_{T2} variable ($M_{T2}(b)$ in our notation) is suboptimal; due to the softness of the leptons, the signal $M_{T2}(b)$ and $M_{2CC}(b)$ distributions lie entirely within the background region. On the other hand, the other three variables perform very well, unlike the case in section 3.3. In particular, the subsystem (ab) variables alone could possibly remove the background with virtually no loss of signal. The subsystem (a) variables are also promising; the use of $M_{2CC}(a)$ seems slightly more effective than the use of $M_{T2}(a)$. Finally, the usual invariant mass, $m_{b\ell}$, allows one to separate signal and background, but the signal loss is more significant for this variable.

The lesson from figures 7 and 9 is that in order to efficiently probe the full mass parameter space of figure 4, one would have to design an analysis which utilizes the full complement of subsystem invariant mass variables, since different variables are optimal in different regions. Of course, one should not overlook the more conventional variables. In
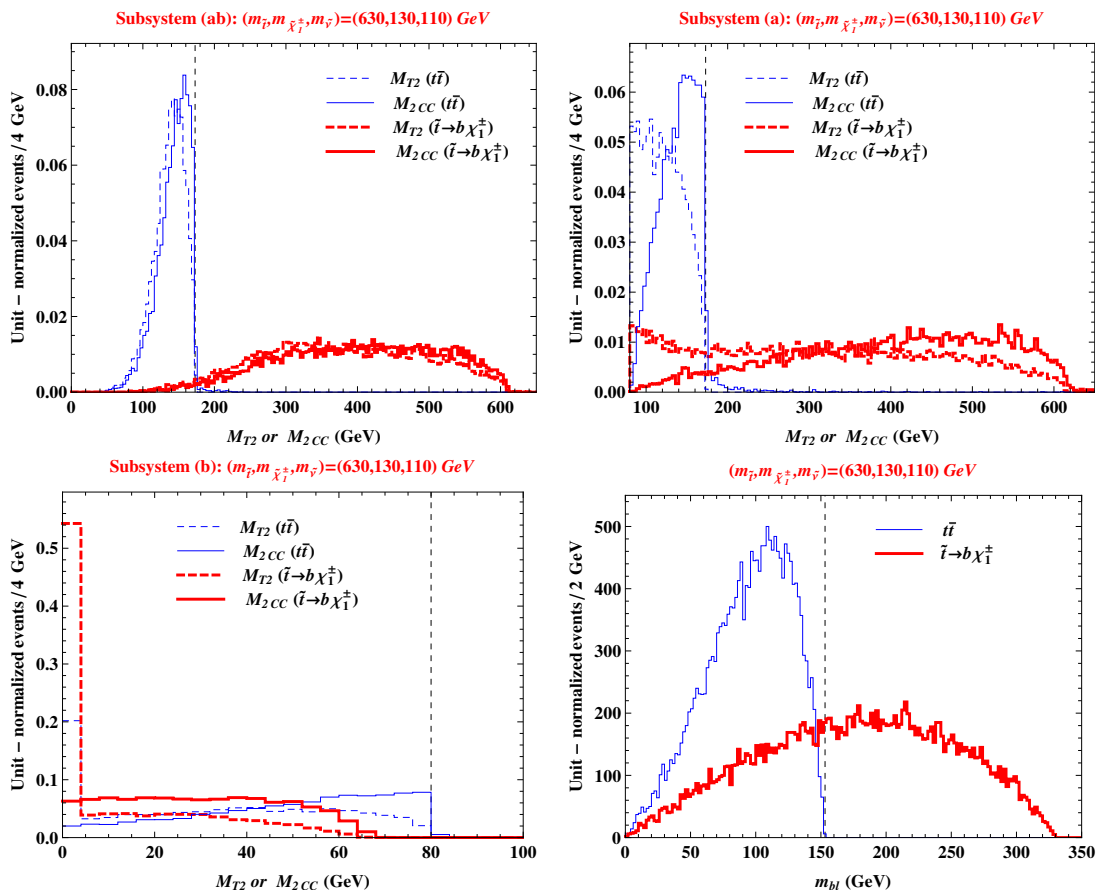
Figure 9. The same as figure 5, but with signal events for study point 3 ($m_{\tilde{t}} = 630\,\text{GeV}$, $m_{\tilde{\chi}^{\pm}} = 130\,\text{GeV}$ and $m_{\tilde{\nu}} = 110\,\text{GeV}$).
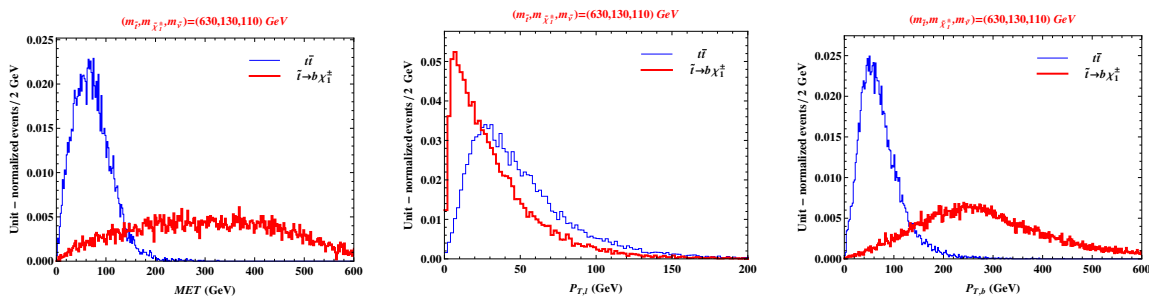

Figure 10. The same as figure 6, but for signal events for study point 3 ($m_{\tilde{t}} = 630\,\text{GeV}$, $m_{\tilde{\chi}^{\pm}} = 130\,\text{GeV}$ and $m_{\tilde{\nu}} = 110\,\text{GeV}$).

figure 10 we show the signal and background distributions of MET, $p_{T,\ell}$, and $p_{T,b}$ for study point 3. As expected, the lepton p_T distribution for the signal is rather soft, but the signal distributions for both MET and $p_{T,b}$ have long tails which extend to the right of the bulk of the corresponding background distribution. This suggests that MET and $p_{T,b}$ could also play a useful role in the analysis.
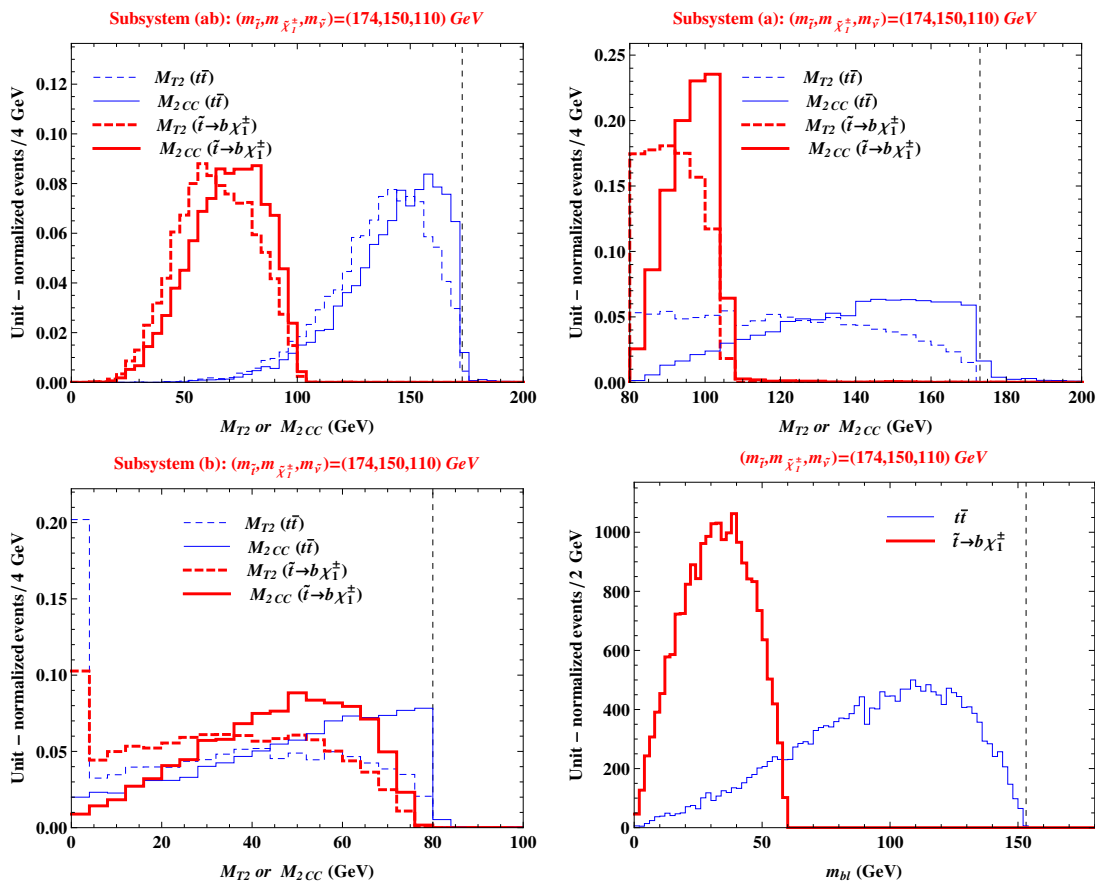
Figure 11. The same as figure 5, but with signal events for study point 4 ($m_{\tilde{t}} = 174\,\text{GeV}$, $m_{\tilde{\chi}^{\pm}} = 150\,\text{GeV}$ and $m_{\tilde{\nu}} = 110\,\text{GeV}$).
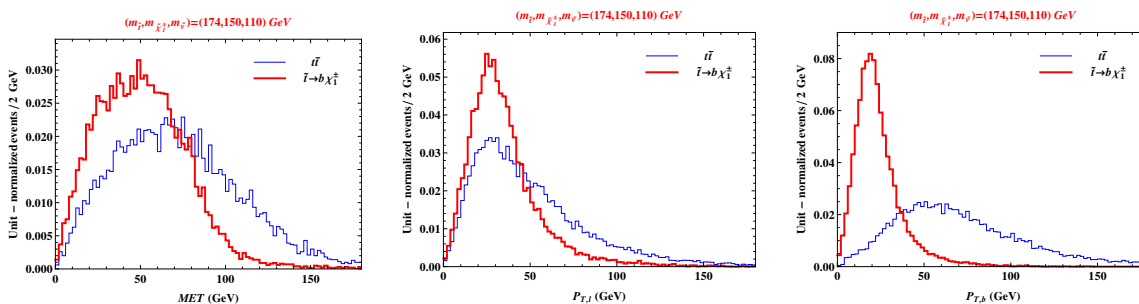

Figure 12. The same as figure 6, but for signal events for study point 4 ($m_{\tilde{t}} = 174\,\text{GeV}$, $m_{\tilde{\chi}^{\pm}} = 150\,\text{GeV}$ and $m_{\tilde{\nu}} = 110\,\text{GeV}$).

3.5 Study point 4: a difficult case in region vi

Our final example for the signal event topology of figure 2(b) is a study point in the most challenging region, vi, where no endpoint violations should occur. The mass spectrum for study point 4 is given in table 3, and the resulting signal and background distributions are displayed in figures 11 and 12. Discovery is clearly challenging in this scenario, as

Study Point	Stop Mass	Neutralino Mass
5	$300\,\mathrm{GeV}$	$100\,\mathrm{GeV}$
6	$174\,\mathrm{GeV}$	$0\,\mathrm{GeV}$

Table 4. The stop and neutralino masses for the two study points considered in this section.

the b-jets will be quite soft, while the lepton p_T and MET distributions for the signal are very similar to those for the background. The invariant mass variables in figure 11 are not particularly helpful either, since the kinematic endpoints of the signal distributions are always below those of the background. Whether stops can be discovered at study point 4 thus remains an open question, which we shall revisit in section 5.

4 M_2 endpoint study for Topology 2

In this section we shall focus on the other symmetric signal event topology in figure 2(c), when both stops decay according to Topology 2 in figure 1(b). The on-shell constrained invariant mass variables discussed in the previous section will be useful here as well, since they were constructed with the *background* topology in mind, which has not changed. Even though the signal event topology is now more complicated (there are two invisible particles in each decay chain), the signal distributions still exhibit kinematic endpoints. We find that the M_{T2} endpoints are given by (see, e.g., [86])

$$M_{T2}^{\max}(ab; \tilde{m} = 0) = 2\, C_+(m_t, m_\nu), \tag{4.1}$$

$$M_{T2}^{\max}(a; \tilde{m} = m_W) = C_+(m_t, m_W) + \sqrt{C_+^2(m_t, m_W) + m_W^2}, \tag{4.2}$$

$$M_{T2}^{\max}(b; \tilde{m} = 0) = 2\,\sqrt{C_+(m_W, m_\nu)\,[C_+(m_W, m_\nu) - C_-(m_t, m_W)]}, \tag{4.3}$$

where

$$C_\pm(x, y) \equiv \frac{x^2 - y^2}{4\, m_{\tilde{t}}\, x^2}\,\left\{ m_{\tilde{t}}^2 + m_t^2 - m_{\tilde{\chi}^0}^2 \pm \sqrt{\lambda\left(m_{\tilde{t}}^2, m_t^2, m_{\tilde{\chi}^0}^2\right)} \right\}, \tag{4.4}$$

$$\lambda(x, y, z) \equiv x^2 + y^2 + z^2 - 2xy - 2yz - 2zx. \tag{4.5}$$

Upon careful examination of eqs. (4.1)–(4.3), one can show that these kinematic endpoints are always above the corresponding background endpoints (2.13)–(2.15), as long as the channel $\tilde{t} \to t\tilde{\chi}^0$ is open (i.e., the decay is kinematically allowed). As we move close to the threshold for $\tilde{t} \to t\tilde{\chi}^0$, the signal kinematic endpoints (4.1)–(4.3) converge to the corresponding SM values (2.13)–(2.15), and discovery becomes very challenging. In this section, therefore, we shall consider two study points: one above this threshold and one at threshold. The mass spectra for those study points are listed in table 4.

4.1   Study point 5: a case above the $\tilde{t} \to t\tilde{\chi}^0$ threshold

We first discuss study point 5, where the mass splitting is large enough that the decay $\tilde{t} \to t\tilde{\chi}^0$ is open, and the resulting top quark is on-shell. The corresponding kinematic distributions are shown in figures 13 and 14. It is clear that this is already a challenging case — the signal and background distributions for the "conventional" variables in figure 14 are
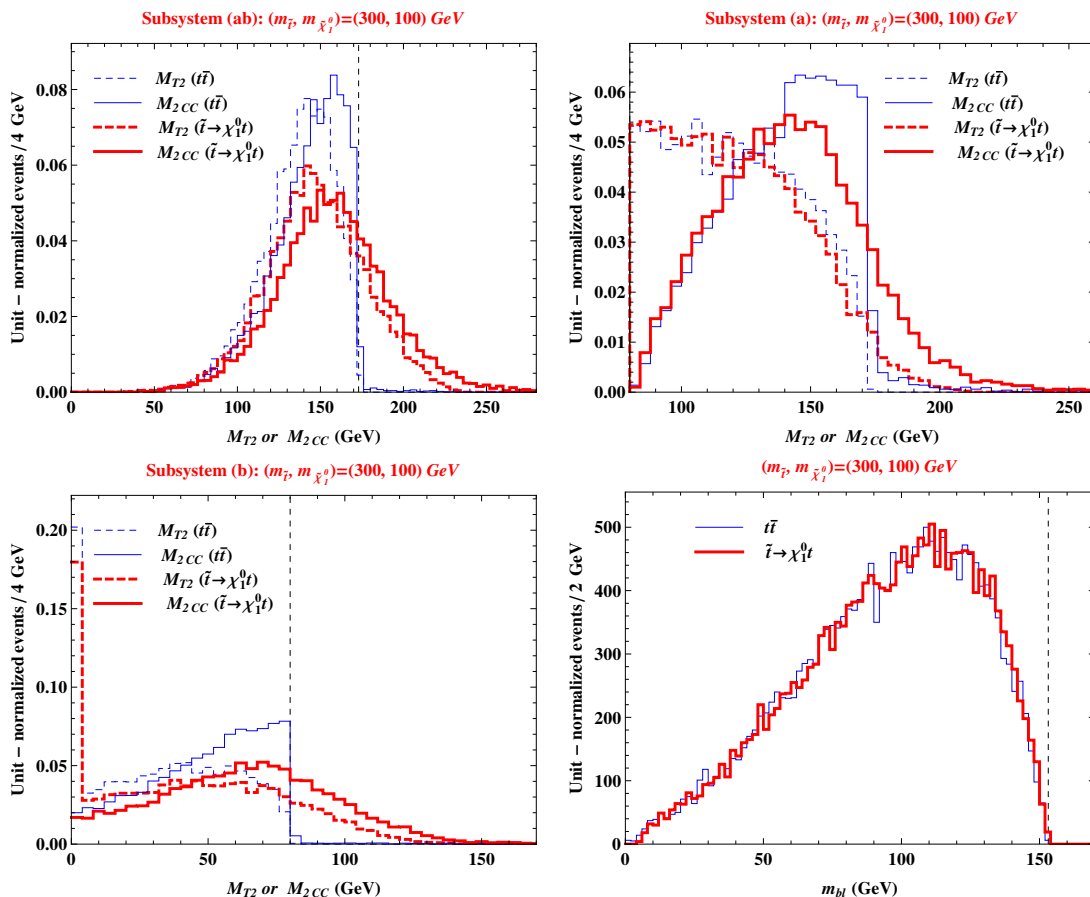
Figure 13. The same as figure 5, but for signal events with the event topology of figure 2(c) for study point 5 ($m_{\tilde{t}} = 300\,\text{GeV}$ and $m_{\tilde{\chi}^0} = 100\,\text{GeV}$).
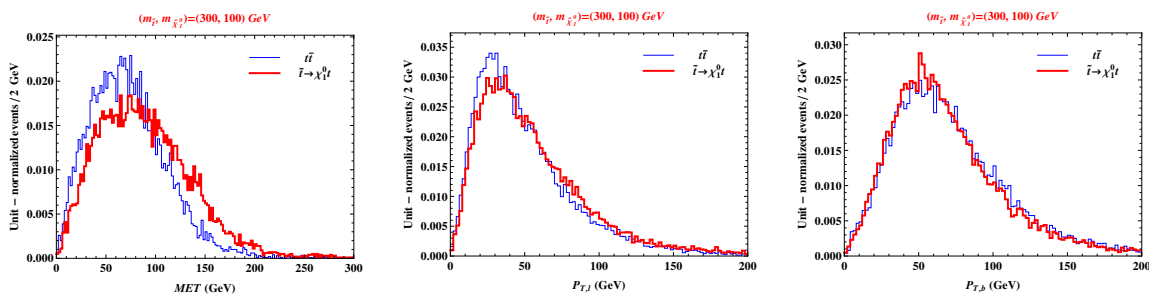

Figure 14. The same as figure 6, but for signal events with the event topology of figure 2(c) for study point 5 ($m_{\tilde{t}} = 300\,\text{GeV}$ and $m_{\tilde{\chi}^0} = 100\,\text{GeV}$).

rather similar. The jet and lepton p_T spectra are governed by the known mass differences between the SM particles t, $W^{\pm}$, and ν, thus, there is very little distinction between the signal and background p_T distributions. Similarly, the $m_{b\ell}$ distribution in figure 13 is the same for signal and background. The MET distribution in figure 14 is slightly harder for the signal, due to the presence of two additional invisible particles. However, the effect is very small and hence unlikely to be useful in practice.

This motivates the use of the M_{T2} and $M_{2\sqcup\sqcup}$ variables whose distributions are shown in the first three panels of figure 13. As anticipated from eqs. (4.1)–(4.3), for all three subsystems (ab), (a), and (b), the signal distributions for the M_{T2} variable have a tail which extends beyond the background endpoints. This effect is most pronounced for subsystem (ab) and less so for subsystem (a).

Note how the situation improves if one were to use the on-shell constrained variable M_{2CC} (solid lines) instead of M_{T2} (dashed lines). For background events, M_{2CC} is computed by applying the correct kinematic constraints; therefore, the kinematic endpoints (2.13)–(2.15) are still obeyed. For signal events, we get a somewhat different story — a much larger fraction of signal events now violate these endpoints, leading to an improvement in the signal efficiency. The largest benefit is observed in the case of subsystem (a), for which previously the M_{T2} variable was the least helpful. There are two separate reasons why M_{2CC} separates signal from background better than M_{T2}:

1. Due to the hierarchy (2.16), the M_{2CC} distributions are harder than the M_{T2} distributions, thus more signal events are expected to migrate above the background endpoint. The shape difference between the M_{2CC} and M_{T2} distributions is especially noticeable in the case of subsystems (a) and (b) in figure 13. Notice, in particular, the completely different shapes of the $M_{T2}(a)$ and $M_{2CC}(a)$ distributions, as well as the disappearance of the big spike at $M_{T2}(b) = 0$.

2. For signal events, the M_{2CC} kinematic endpoints themselves are even higher[9] than the M_{T2} kinematic endpoints given in eqs. (4.1)–(4.3). This can be readily observed in figure 13, where the signal M_{2CC} distributions (red solid lines) extend to higher values than the signal M_{T2} distributions (red dashed lines). Contrast this situation with the examples considered in section 3, when M_{T2} and M_{2CC} always shared the same kinematic endpoint. There, the signal event topology (figure 2(b)) was the same as the background event topology (figure 2(a)). As a result, the kinematic constraints being imposed in the calculation of M_{2CC} did correspond to the actual physics of the signal events. Now, in the case of study point 5, the signal event topology of figure 2(c) is completely different — in a sense, one is applying "the wrong" constraints when calculating M_{2CC}. Somewhat paradoxically then, figure 13 teaches us that one obtains a beneficial result, despite applying "the wrong" constraints.

4.2 Study point 6: a case at the $\tilde{t} \to t\tilde{\chi}^0$ threshold

Our last example is a very difficult one: study point 6 in table 4. Here the new physics mass spectrum is such that the decay $\tilde{t} \to t\tilde{\chi}^0$ occurs exactly at threshold. As a result, the (massless) neutralinos carry away a negligible amount of momentum, and the signal events look very top-like. This is illustrated in figures 15 and 16, where we compare our standard set of kinematic distributions for signal and background.

Figure 16 shows that the p_T distributions and the MET distribution are almost identical for signal and background. The invariant mass distributions from figure 15 are also

---

[9]We have not attempted to obtain analytical formulas analogous to (4.1)–(4.3) for the M_{2CC} kinematic endpoints, but our numerical studies clearly showed that the bounds (4.1)–(4.3) themselves are violated in the case of the M_{2CC} variable.
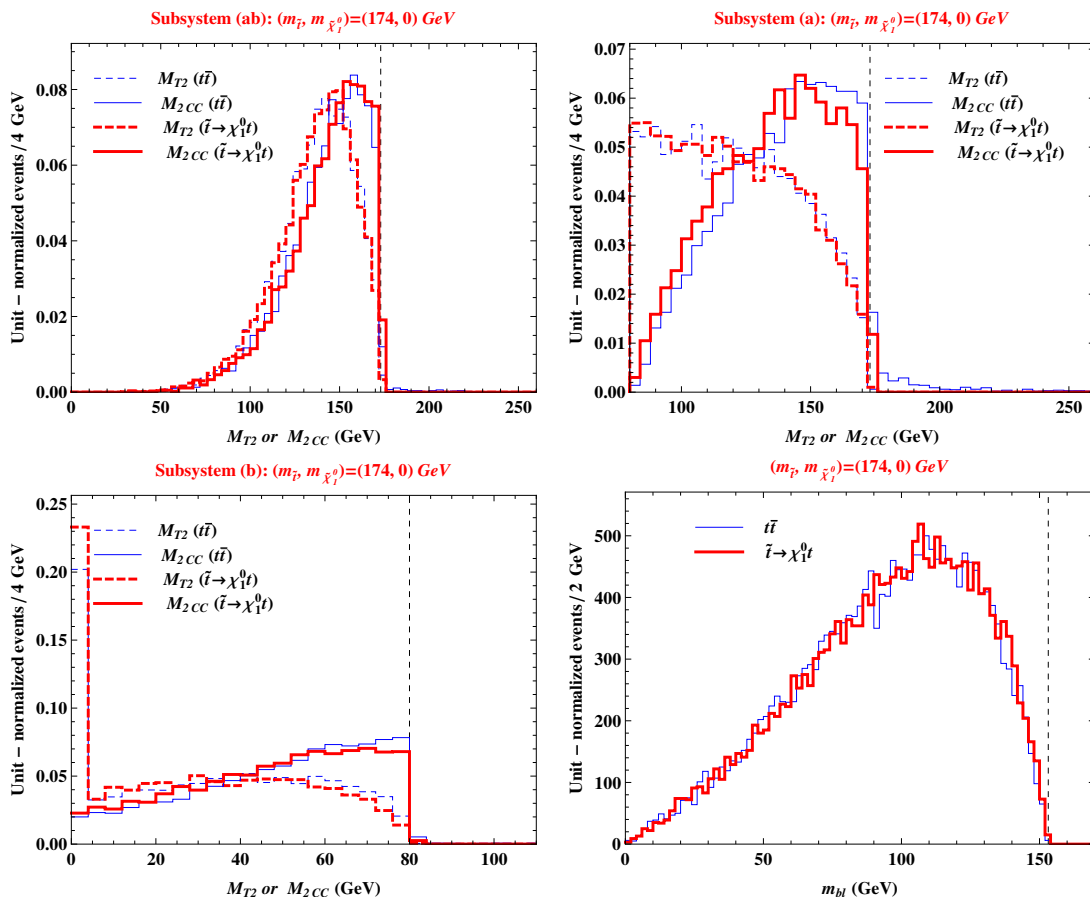
Figure 15. The same as figure 5, but for signal events with the event topology of figure 2(c) for study point 6 ($m_{\tilde{t}} = 174\,\text{GeV}$ and $m_{\tilde{\chi}^0} = 0\,\text{GeV}$).
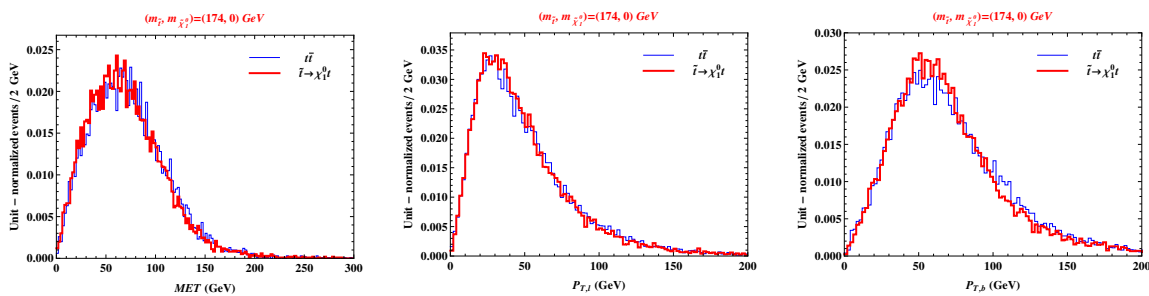

Figure 16. The same as figure 6, but for signal events with the event topology of figure 2(c) for study point 6 ($m_{\tilde{t}} = 174\,\text{GeV}$ and $m_{\tilde{\chi}^0} = 0\,\text{GeV}$).

very similar; there are slight differences in the shapes due to the top quarks in the signal being more likely to be off-shell, but the kinematic endpoints are the same. Thus, barring a shape-based analysis, there are no obvious cuts which could discriminate signal from background. Therefore, just like study point 4, this would be a very difficult, and most likely impossible, scenario for discovery using these methods. As before, we shall leave this as an open question to be revisited in section 5.

5 M_2 endpoint study for mixed events

In this section, we shall consider signal events with the mixed event topology of figure 2(d). In doing so, we are motivated by two factors:

- In any realistic model, the stop is likely to have several relevant decay modes. (Here we consider the simplest scenario with only the two decay modes from figure 1.) Since the stops are pair-produced, the number of signal events in each symmetric channel is proportional to the corresponding branching ratio squared. For mixed events, where the two stops decay *differently*, the number of signal events benefits from an additional combinatorial factor of 2.

- In the course of our study of the symmetric event topologies from figure 2(b) (in section 3) and figure 2(c) (in section 4), we determined that there are "blind spots" in the mass parameter space, where the signal resembles the background, and discovery is very challenging. Study points 4 and 6 are examples of such difficult cases. In this section, therefore, we shall investigate the question of whether one can recover some sensitivity by considering mixed events constructed from precisely those two difficult cases. In other words, we consider events with the event topology of figure 2(d), where the upper (lower) decay chain corresponds to study point 4 (study point 6). (Study point 4 gives the stop mass (174 GeV) and the neutralino mass (0 GeV); study point 6 uses the same stop mass, a chargino mass of 150 GeV and a sneutrino mass of 110 GeV.) We shall assume that the two stop decays occur with equal branching fractions.

The idea to use mixed stop events was previously discussed in ref. [65], which suggested a new variable, "topness", that quantifies how well an event can be reconstructed under the top background hypothesis. In order to calculate the "topness" of an event, one minimizes the total $\sqrt{s}$ of the event, making the reasonable ansatz that the momentum configuration thus obtained provides a good approximation to the true kinematics of the event [65, 103]. Our approach is similar to the extent that the on-shell constrained invariant mass variables, like M_{2CC}, are also found by minimization, though not of the total $\sqrt{s}$ but of the parent mass in the respective subsystem. By imposing the symmetry constraints (2.4) and (2.7), we focus on the one key difference between the signal and background events: the signal event topology is asymmetric while the background event topology is symmetric. We can therefore expect that the constraints (2.4) and (2.7) will affect signal and background events *differently*.

As a point of reference, we begin by showing distributions of variables for which no improvement can be expected in the case of mixed events in figure 17. The four variables depicted in the figure are the three subsystem M_{T2} variables and the invariant mass $m_{b\ell}$. All four variables are calculated here using the assignment of the leptons and b-quarks to the correct decay chains. Each panel contains four distributions, one for each event type from figure 2: the $t\bar{t}$ background from figure 2(a) (blue dot-dashed lines); the symmetric $\tilde{t} \to b\tilde{\chi}_1^+$ signal events from figure 2(b) (magenta dotted lines); the symmetric $\tilde{t} \to t\tilde{\chi}_1^0$
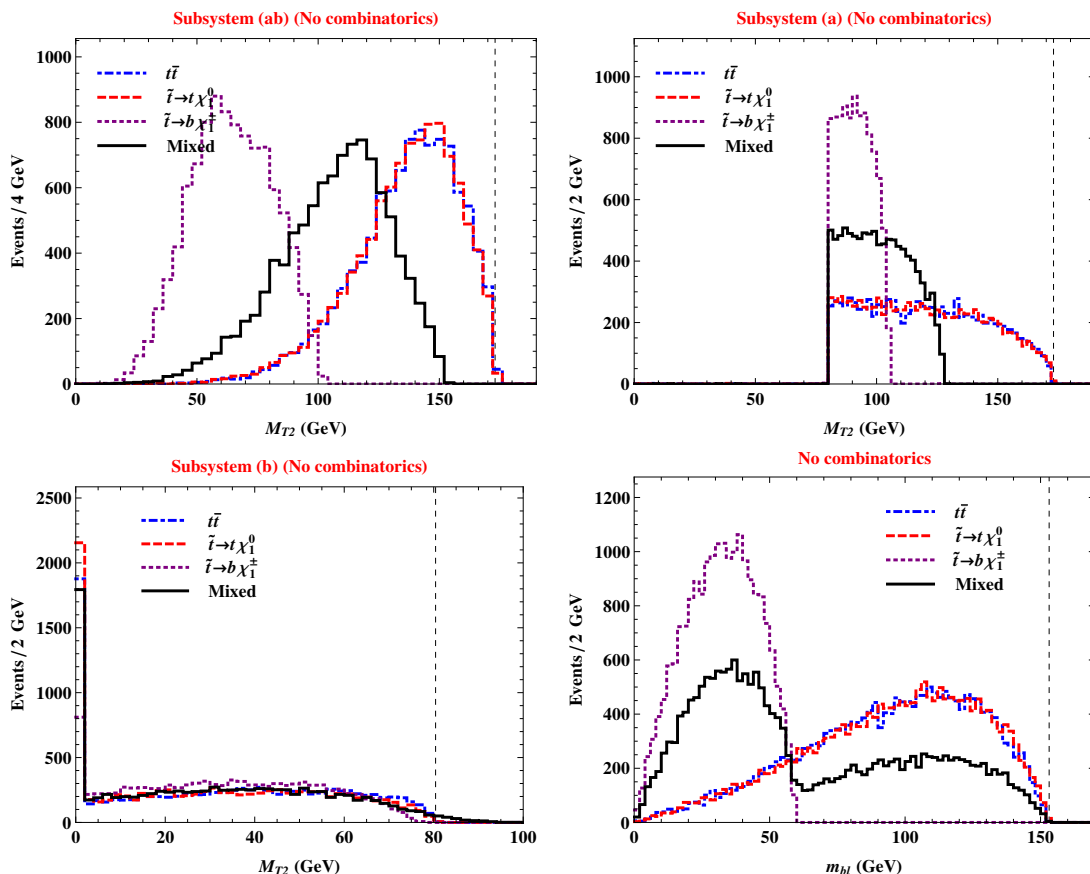
Figure 17. The same as figures 11 and 15, comparing distributions of the three M_{T2} subsystem variables and the invariant mass $m_{b\ell}$ for the four types of events in figure 2. The mass spectrum corresponds to study points 4 and 6: $m_{\tilde{t}} = 174\,\text{GeV}$, $m_{\tilde{\chi}^\pm} = 150\,\text{GeV}$, $m_{\tilde{\nu}} = 110\,\text{GeV}$, and $m_{\tilde{\chi}^0} = 0\,\text{GeV}$.

signal events from figure 2(c) (red dashed lines); and the asymmetric signal events from figure 2(d) (black solid lines). The vertical black dashed line in each panel marks the location of the upper kinematic endpoint of the $t\bar{t}$ background distribution. We see that for all three types of signal events (symmetric or asymmetric), the respective distributions do not violate the background kinematic endpoints, thus discovery appears to be just as difficult with mixed events as it was with the symmetric events considered earlier in sections 3.5 and 4.2. This conclusion is easy to understand; the M_{T2} variable is a variable defined on the transverse plane, where it is impossible to impose a 3+1-dimensional mass constraint like eq. (2.4) or (2.7).

The situation is quite different when we consider distributions of on-shell constrained variables, M_{2CC}, for which the constraints of eqs. (2.4) or (2.7) are imposed. As seen in figure 18, the signal distributions for mixed events may now exhibit endpoint violation, even when the signal distributions for symmetric events do not. The effect is most pronounced in the case of the subsystem variable $M_{2CC}(b)$; for the subsystem variable $M_{2CC}(ab)$ it is less noticeable, while for $M_{2CC}(a)$ it is absent altogether. Figure 18 showcases the main
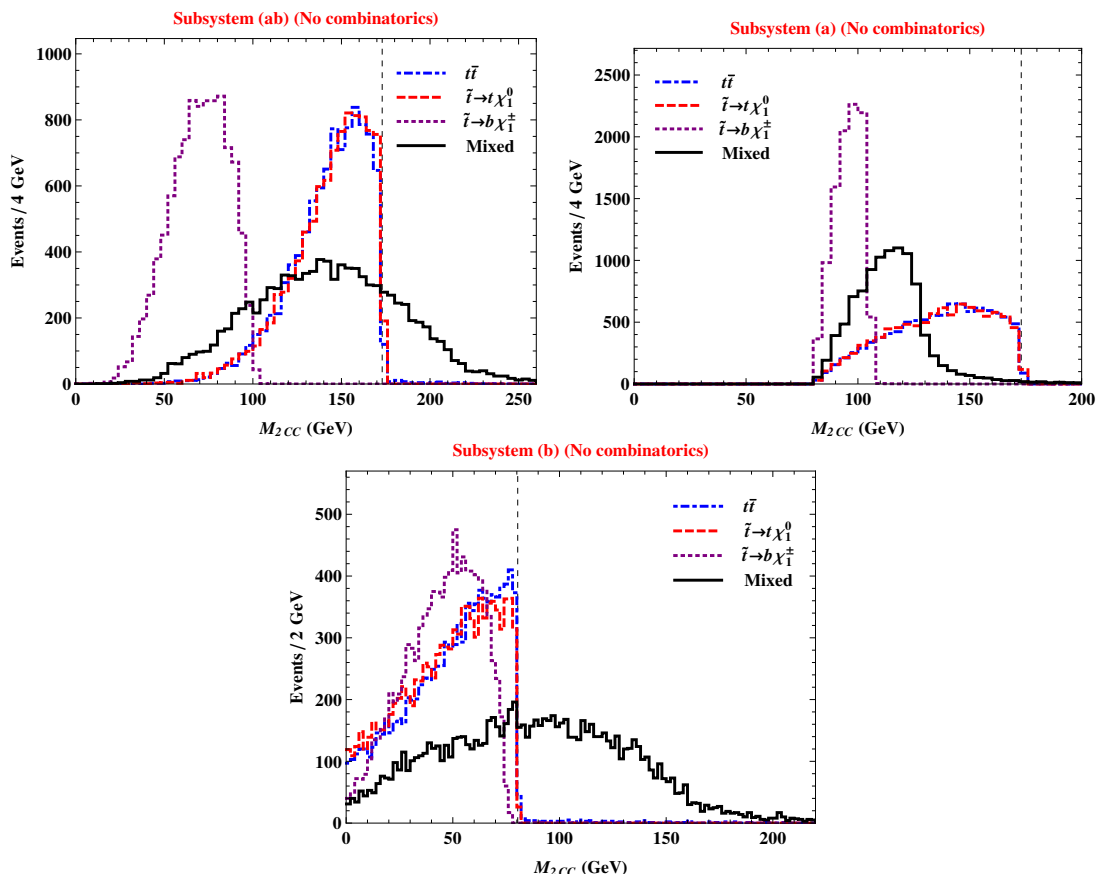
Figure 18. The same as figure 17, but for the on-shell constrained variable M_{2CC} in the three possible subsystems (ab), (a), and (b).

result of this section: that with the help of an appropriately chosen on-shell constrained variable (in this case $M_{2CC}(b)$), one can obtain a relatively good separation of signal from background *for mixed events*. It is worth emphasizing that this separation was achieved for a very unfavorable choice of mass parameters, as the study points 4 and 6 were not observable using events where both decay chains had the same topology.

Given that endpoint violation was observed for both $M_{2CC}(b)$ and $M_{2CC}(ab)$, it is worth investigating the possible correlation between those two variables. In figure 19 we show two-dimensional plots exhibiting those correlations. We consider separately the three types of signal events: pure Topology 1 from figure 2(b) (upper left), pure Topology 2 from figure 2(c) (upper right), and the mixed topology from figure 2(d) (lower left). Finally, the lower right panel in figure 19 shows the result for the full signal sample, with equal branching fractions for Topology 1 and Topology 2. The black dashed lines in figure 19 mark the locations of the expected upper kinematic endpoints for background events, following eqs. (2.15) and (2.13). Any events which appear to the right of the vertical black dashed lines and/or above the horizontal black dashed lines in figure 19 are expected to be signal-like. In agreement with figure 18, we see that for symmetric signal event topologies (the upper two panels in figure 19), the signal events are contained within
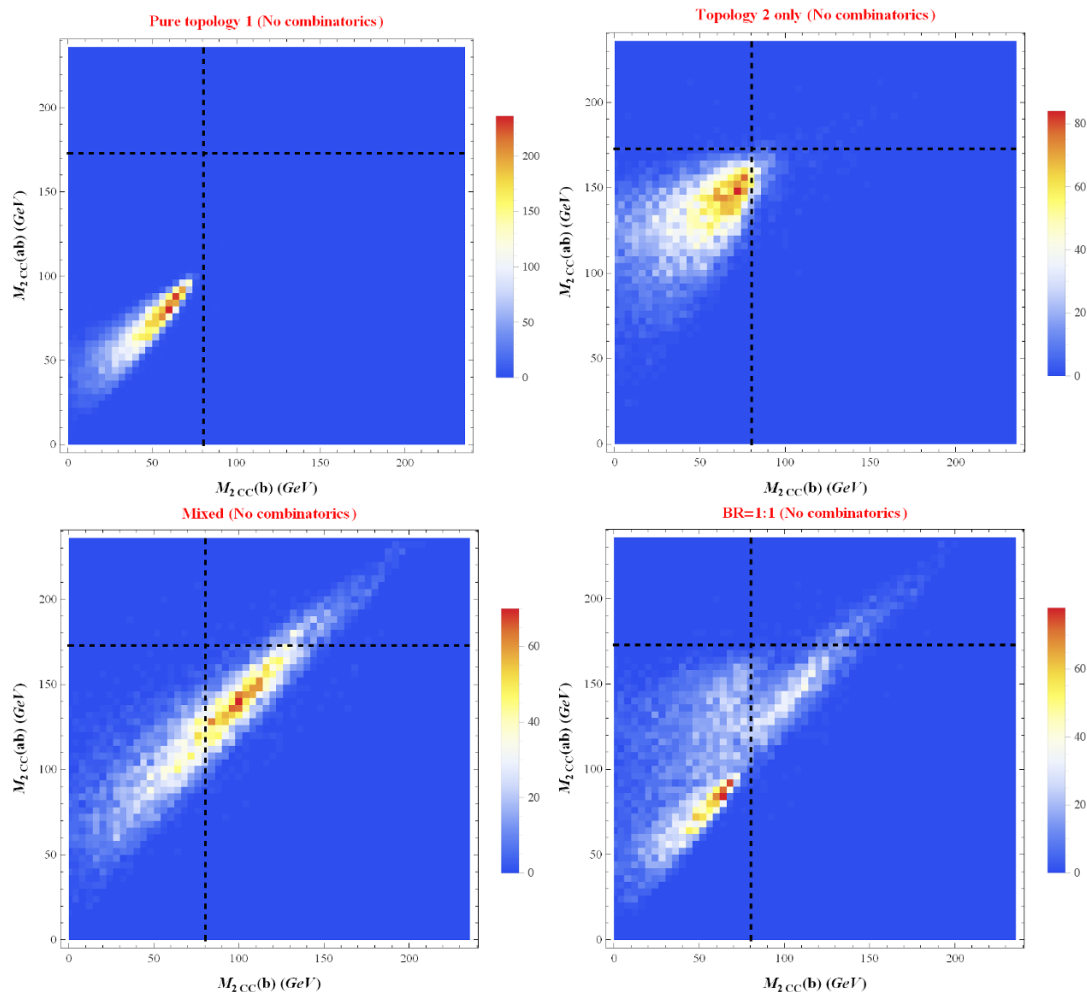
Figure 19. The correlation between the two best performing variables from figure 18, for the three types of signal events: pure Topology 1 from figure 2(b) (upper left), pure Topology 2 from figure 2(c) (upper right), mixed topology from figure 2(d) (lower left), and combined total (lower right).

the "background-like" rectangular region adjacent to the origin. On the other hand, for the asymmetric event topology of figure 2(d) (the lower left panel), many signal events leak out of the background-like box. The figure also reveals a linear correlation between $M_{2CC}(b)$ and $M_{2CC}(ab)$. Furthermore, the slope is such that if an event violates the background $M_{2CC}(ab)$ endpoint (2.13), it also necessarily violates the background $M_{2CC}(b)$ endpoint (2.15), while the reverse is not true. We therefore conclude that the $M_{2CC}(b)$ distribution alone is sufficient in separating signal from background in this scenario with mixed events.

In our discussion so far in this section, we have been ignoring the combinatorial problem arising when we try to pair up the two b-jets with the two leptons. Since the b-quark charge is not measured, we have two possible pairings, each resulting in a candidate value for the kinematic variable. Since we are interested in upper kinematic endpoints, the simplest solution is to consider both pairings and then pick the one which gives the *smaller*
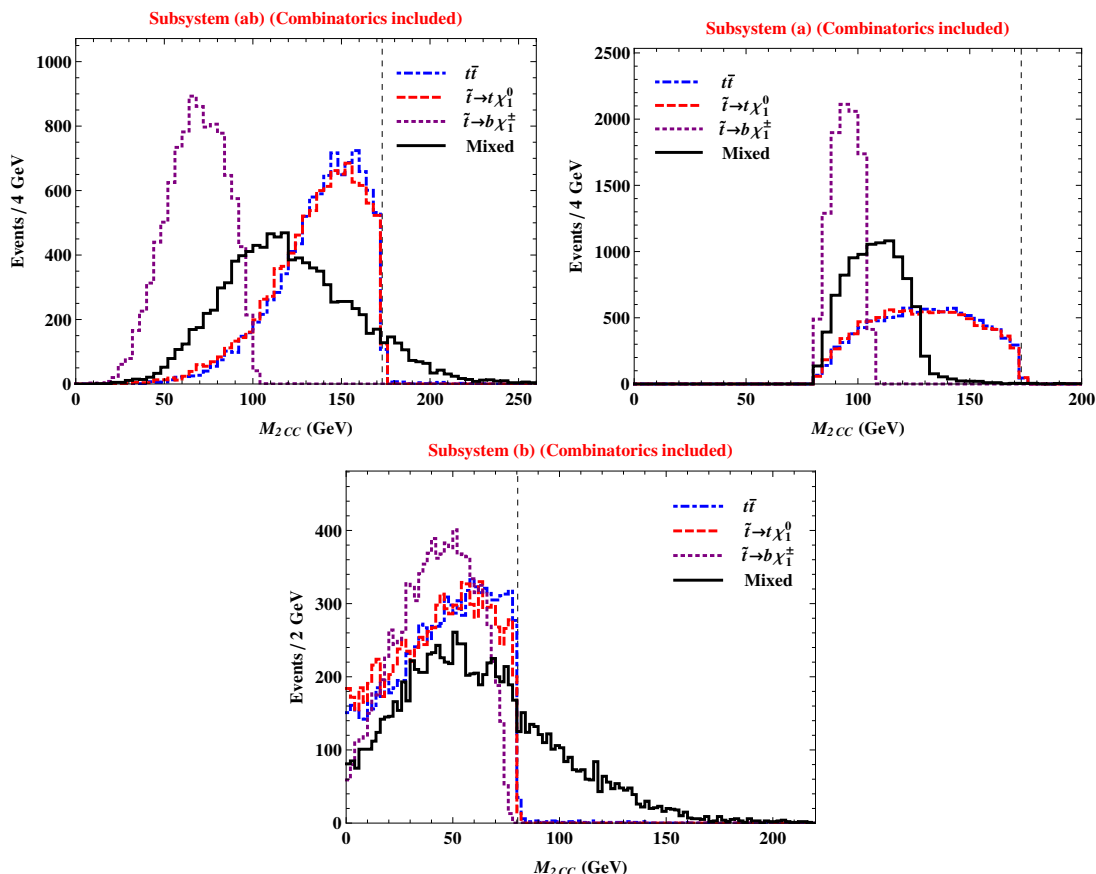
Figure 20. The same as figure 18, but including the effects of combinatorics: for each event, we try both possible assignments of the lepton-b pairs, and plot the smaller of the two resulting M_{2CC} values.

value for the kinematic variable. This approach has been followed in recreating figures 18 and 19 as figures 20 and 21, respectively. As expected, this procedure tends to shift all distributions towards lower values, thus the number of signal events which violate the background endpoints is fewer than before; compare, e.g., the $M_{2CC}(b)$ distributions for mixed events in figures 18 and 20. Nevertheless, the effect is still present, offering hope that difficult cases like study points 4 and 6 could perhaps best be looked for in such mixed event topologies instead.

6 Results with realistic detector simulation

In the previous three sections we saw that the M_{T2} and M_{2CC} variables allow us to identify signal events as tails which extend beyond the upper kinematic endpoint for background events. However, in a realistic experiment, the background distributions themselves may acquire high tails, for a variety of reasons. This is why it is necessary to test our previous observations, which were made at parton level, with realistic simulation, including the effects of detector resolution, initial and final state radiation, jet reconstruction, cuts, etc.
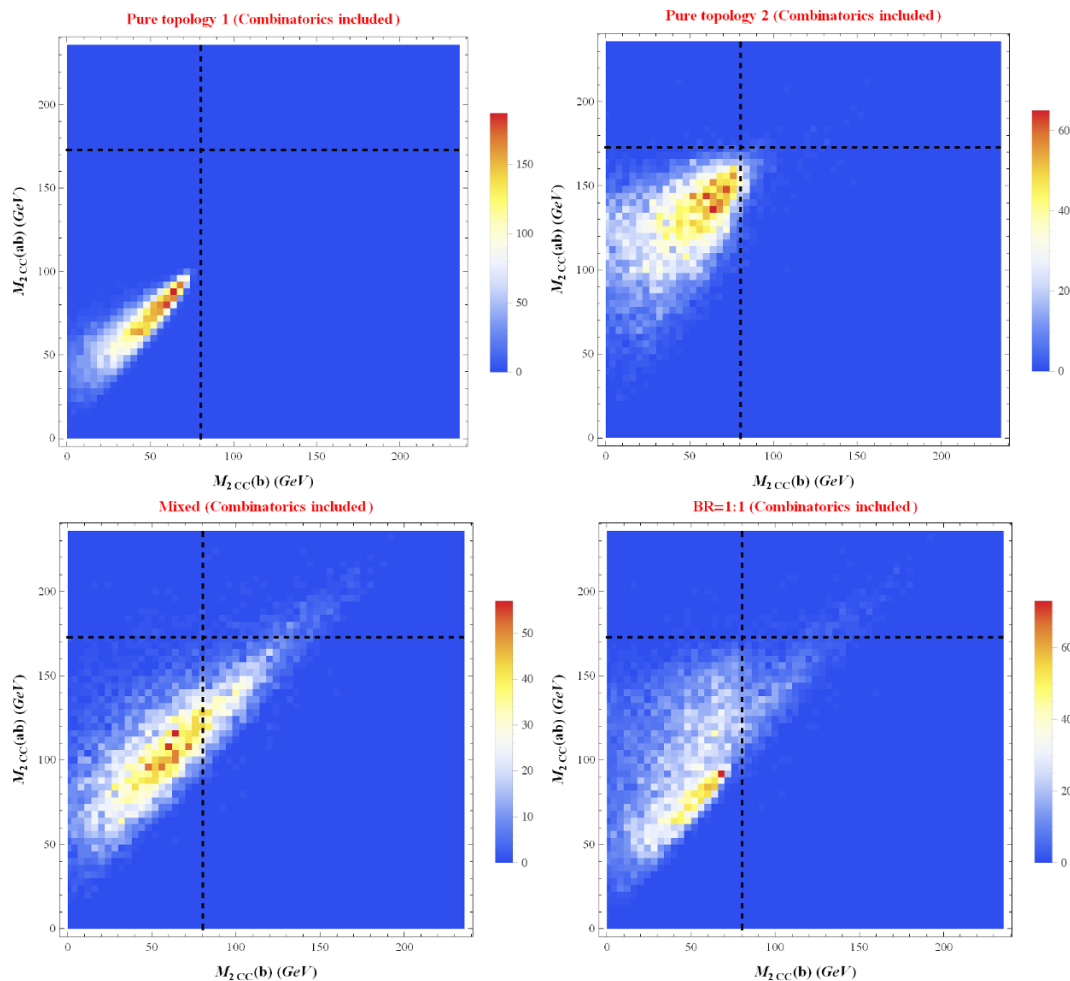
Figure 21. The same as figure 19, but including the effects of combinatorics as in figure 20.

It is clear that our positive conclusions drawn for fortuitous cases of new physics like study point 1 will survive all these complications, therefore in this section we shall only focus on the difficult scenario discussed in section 5, i.e., the mixed events which were a hybrid between the difficult study points 4 from section 3.5 and 6 from section 4.2.

6.1 Event simulation details

As before, the parton-level event generation is done by `MadGraph_aMC@NLO` [104], where by default the parton distributions are evaluated by `NNPDF23` [105]. The relevant output is then piped through `Pythia 6.4` [106] and `Delphes3` [107]. For both signal and $t\bar{t}$ background, the decays of top quarks are handled by `Pythia 6.4`, while Topology 1 is explicitly generated by `MadGraph_aMC@NLO` without any prior cuts. All simulations are performed at leading order for a pp collider of $\sqrt{s} = 14\,\mathrm{TeV}$.

For the signal process, we assume that the branching ratio of Topology 1 relative to Topology 2 is 1 : 1. In addition, in Topology 1, the chargino is forced to decay exclusively into a sneutrino (which may further decay invisibly), and a lepton (i.e., electron and muon

only). In Topology 2, the stop decays to the lightest neutralino and a top quark, which subsequently decays with the relevant branching ratios predicted in the SM. For our purposes, we only consider the dilepton final state, in which both top quarks decay leptonically. The input top quark mass is set to $173\,\mathrm{GeV}$, while the $W^{\pm}$ gauge boson mass is $80\,\mathrm{GeV}$. Jets are reconstructed with the anti-k_t algorithm [108], using a radius parameter $R = 0.5$. The b-tagging efficiency is taken to be 70%, while light quark jets are mis-tagged at the rate of 1%.

Given the final state $2b + 2\ell + \not{E}_T$, in principle there are several sources of SM background that need to be taken into account. In order to suppress the reducible SM backgrounds, we apply the following pre-selection cuts:

- The event must contain exactly two opposite sign leptons with $p_T > 10\,\mathrm{GeV}$ and $|\eta| < 2.5$ ($|\eta| < 2.4$) for electrons (muons).

- In order to reduce background from low mass resonances, in the ee and $\mu\mu$ channels, we demand $m_{ee/\mu\mu} > 20\,\mathrm{GeV}$. Furthermore, to reduce the Z+jets background, events with dilepton masses within the Z-mass window are vetoed by requiring $|m_{ee/\mu\mu} - m_Z| > 15\,\mathrm{GeV}$.

- To further suppress Drell-Yan, for the ee and $\mu\mu$ channels, we apply a missing transverse energy cut of $\not{E}_T > 40\,\mathrm{GeV}$.

- The event is required to have ≥ 2 jets with $p_T > 30\,\mathrm{GeV}$ and $|\eta| < 2.4$. It is also required that exactly two of these jets are b-tagged.

After these cuts, we are left with $t\bar{t}$ as the dominant (irreducible) background, and this will be the only background process we will consider here. The posterior cuts using M_2 variables are imposed for events already passing the above set of pre-selection cuts.

6.2 Results for M_{T2} and M_{2CC}

We first revisit our results from section 5, this time including the effects of detector simulation and combinatorics. As before, we consider both pairings of the two tagged b-jets and the two leptons, and use the *smaller* of the two resulting values for the kinematic variable under consideration. However, unlike the plots in section 5, here we do not separate the three types of signal events (Topology 1, Topology 2 and mixed), since in the real experiment there is no way to tell which is which.

Figure 22 compares the signal and $t\bar{t}$ background distributions for the three different M_{T2} subsystem variables. As expected from the parton-level results in section 5 (see figure 17), the discrimination power in the high tail region is relatively poor, since the signal and the background events obey the same kinematic endpoints.

Figure 23 shows the corresponding M_{2CC} distributions for signal and $t\bar{t}$ background events in the three subsystems. As anticipated from the parton-level result in figures 18 and 20, there is a noticeable improvement in the (b) subsystem (for which the visible particle is a lepton) as seen in the lower panel and a slight improvement in the (ab) subsystem as well. Therefore, one would expect that a minimum M_{2CC} cut would be beneficial. The optimal value of the cut would depend on the expected signal cross-section, and on the assumed systematic uncertainty on the background normalization in the high tail region.
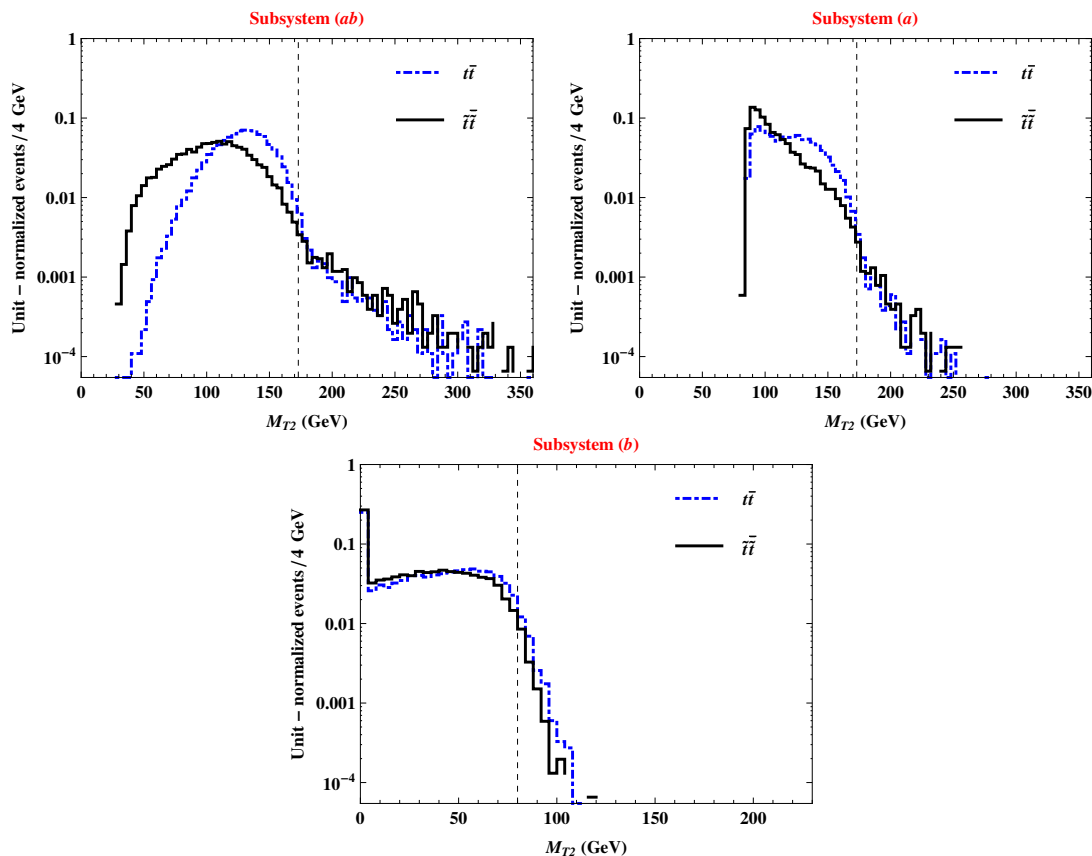
Figure 22. The same as figure 17, but including the effects of combinatorics and detector simulation. The vertical black dashed lines denote the expected M_{T2} endpoints of the $t\bar{t}$ background in each subsystem.

A careful comparison of the parton-level results in figures 17, 18 and 20 versus the detector-level results in figures 22 and 23 reveals that at the detector level the background distributions develop high tails which, unless properly understood, could be confused with a signal. We have checked that in the majority of cases, background events populate the high tail due to imperfect b-tagging. A typical event looks as follows: one of the two b-jets is either too soft to pass the jet ID cuts, or is not tagged as a b-jet. (Recall that the b-jet tagging inefficiency is 30%.) Instead, a gluon from initial state radiation (ISR) forms a hard jet which is subsequently mistagged as a b-jet. Thus in computing the M_{T2} and M_{2CC} variables one is using the wrong b-jet object, which leads to the endpoint violation. An improvement in the b-tagging algorithm, especially one which lowers the mistag rate for ordinary QCD jets, would help alleviate this problem.

6.3 Results for the relative shift from M_{T2} to M_{2CC}

In all of our analysis so far, we have relied on the existence of the background kinematic endpoints (2.13)–(2.15) and focused on the high tails *above* those endpoints. Ideally, this kinematic region should be populated only by signal events, even when one accounts for
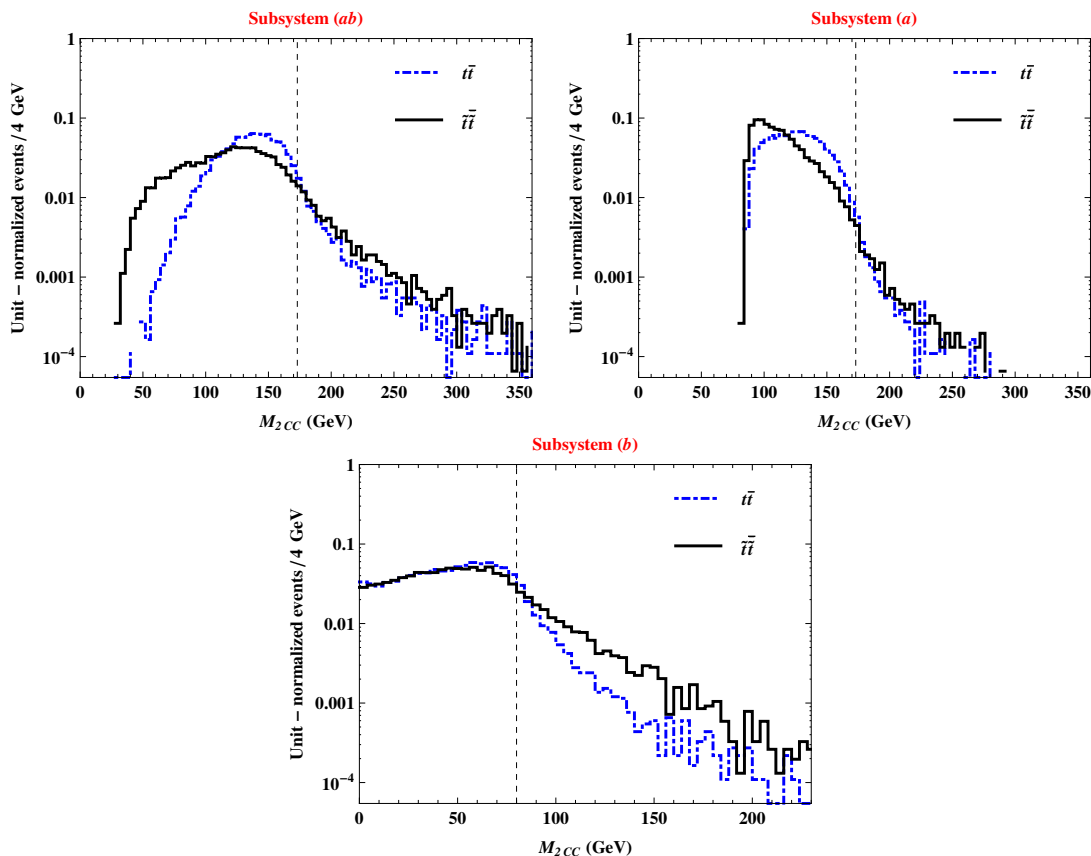
Figure 23. The same as figure 22, but for the corresponding M_{2CC} variables.

the two-fold combinatorial ambiguity in pairing the leptons and the b-jets. Unfortunately, as we have already seen, this straightforward approach has two drawbacks:

- *Presence of high tails in the background distributions.* While in theory the background distributions are not supposed to extend beyond their kinematic endpoints, in practice this is not always the case. Such tails were readily observed in figures 22 and 23, which were obtained using realistic detector simulation.

- *Low signal efficiency.* Unless we are dealing with a new physics model with a widely split spectrum (see related discussion in section 3.1), a significant fraction of the signal events will also lie below the background kinematic endpoints, thus by cutting at or near the endpoint, we will be removing a large chunk of signal events as well. This was very evident in the "worst case" scenarios like study points 4 and 6, or the mixed event case discussed in sections 5 and 6.2.

These two problems suggest that we should reexamine the region *below* the background kinematic endpoints and search for a good discriminating variable which would be applicable to that region as well. As in section 5, our goal will be to target signal events with the mixed event topology of figure 2(d).

To begin with, recall the main difference between the background events described by figure 2(a) and the signal described by figure 2(d): the background events are symmetric while the signal events are asymmetric. The on-shell constrained variables M_{2CX}, M_{2XC}, and M_{2CC} are obtained by applying the additional constraints of eqs. (2.4) and (2.7), which assume that the events are symmetric. Enforcing these constraints leads to the hierarchy (2.16) which is simply due to the fact that a constrained minimum is larger than an unconstrained minimum. Since the background events are symmetric, the constraints (2.4) and (2.7) will be satisfied for the *true* values of the invisible momenta, and, as long as the global minimum is not too far away (in momentum space), one can expect a relatively mild hierarchy (2.16). Conversely, for signal events with the mixed event topology, the *true* values of the invisible momenta in general do not satisfy the constraints (2.4) and (2.7). Thus one could expect that the effect of imposing the constraints would be larger, leading to a larger hierarchy (2.16).

These intuitive considerations suggest that we look at the shift of the on-shell constrained invariant mass variable which is caused by the constraint itself. Keeping in mind the identity $M_{T2} = M_{2XX}$ [87], we can take the usual stransverse mass M_{T2} as our benchmark variable in the absence of any constraints. Then, we can "measure" the effect of the constraints by comparing M_{T2} to M_{2CC}, where both (2.4) and (2.7) have been applied. This motivates the consideration of a new variable[10]

$$\Delta M(S; \tilde{m}) \equiv \sqrt{M_{2CC}^2(S; \tilde{m}) - M_{T2}^2(S; \tilde{m})}. \tag{6.1}$$

As indicated in (6.1), this variable can be computed for any of the three subsystems. We have checked that in our example here, the (ab) subsystem shows the best discrimination between the signal and $t\bar{t}$ background. Therefore, in figure 24, we contrast the new variable $\Delta M(ab)$ defined in (6.1) with the variable $M_{2CC}(ab)$ advocated above in section 5. Each panel in figure 24 shows a specific type of events at parton level: $t\bar{t}$ background events (upper left panel), signal events with pure Topology 1 from figure 2(b) (upper right panel), signal events with pure Topology 2 from figure 2(c) (lower left panel), and signal events with mixed topology from figure 2(d) (lower right panel). We see that, as already observed in figure 18, a certain number of signal events in the mixed channel exceed the background endpoint for M_{2CC}. More importantly, the figure also shows that there are many more signal events which do *not* exceed the background endpoint, yet their value for ΔM is significantly larger than that for a typical background event. The situation does not change much if we account for the two-fold combinatorial ambiguity, as demonstrated by figure 25. We conclude that ΔM possesses additional discriminating power, and therefore, for an optimal analysis, one should use *both* ΔM and M_{2CC} as discriminating variables.

For completeness, we also present results for the ΔM variable alone. Figure 26 shows unit-normalized distributions for $\Delta M(ab)$ at the parton level (upper row) and after detector simulation and selection cuts (lower row). The upper left panel is done with perfect assignment for the lepton–b-jet pairing, while the upper right panel accounts for the two-fold combinatorial ambiguity as before. The lower right panel shows the observable total

---

[10]Since the shift $M_{2CC} - M_{T2}$ is relatively small compared to the individual values of M_{2CC} or M_{T2}, in eq. (6.1) we prefer to define ΔM in terms of the difference of the *squared* masses. The square root is then used merely to lower the mass dimension of ΔM back to GeV.
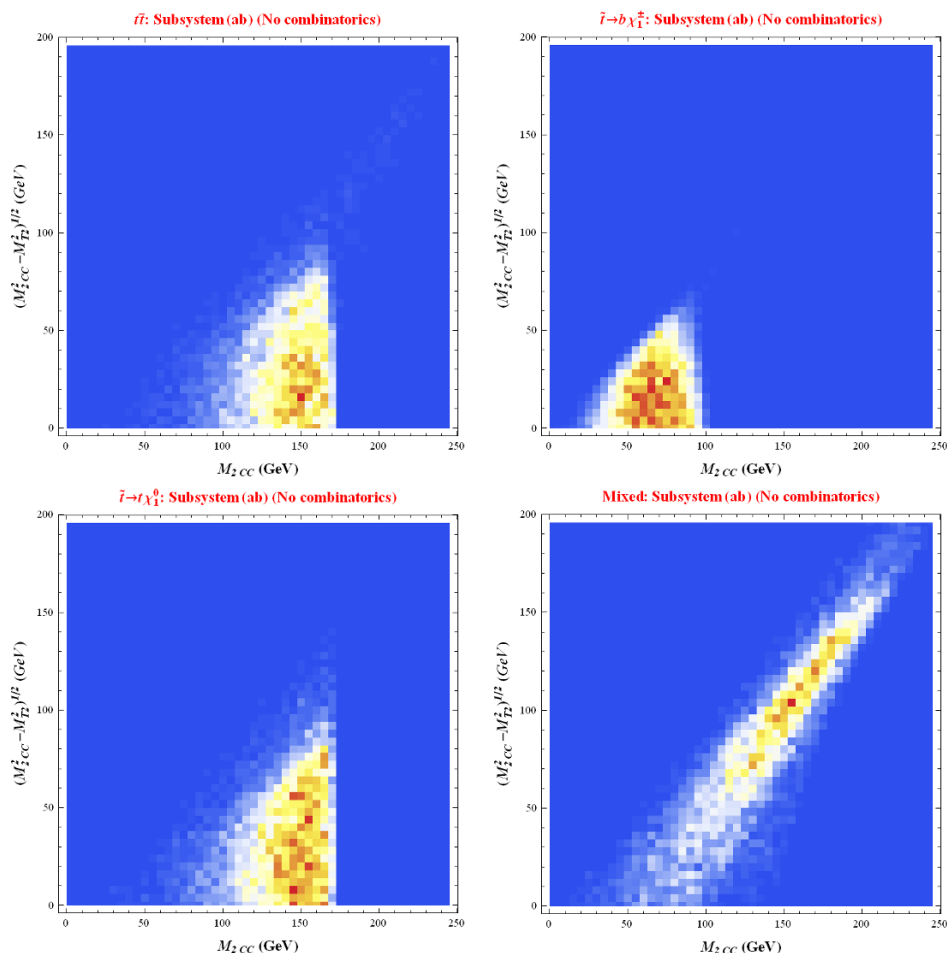
Figure 24. Density plots exhibiting the correlations between the variables $\Delta M(ab)$ and $M_{T2}(ab)$ for background events (upper left) and for the three types of signal events: with pure Topology 1 from figure 2(b) (upper right), pure Topology 2 from figure 2(c) (lower left), and the mixed topology from figure 2(d) (lower right).

signal distribution, which is made up of the individual components identified on the lower left panel. Clearly, the variable $\Delta M(ab)$ performs quite well for signal events with a mixed event topology, and to some extent for signal events with Topology 1. The effect is diluted, but still visible after detector simulation (panels in the lower row).

6.4 An alternative variable: the "relative" mass difference

In the previous section, we proposed the variable, ΔM, as a measure of the effect of the constraints (2.4) and (2.7). The idea was to look at the change in the value of M_2 as a result of enforcing these constraints. Let us now look at a different way of capturing the same effect.

Recall that as a result of the minimization involved in calculating the *unconstrained* M_{2XX} variable, one obtains values for the invisible momenta that minimize the maximal parent particle invariant mass in the specified subsystem. While these are not necessarily
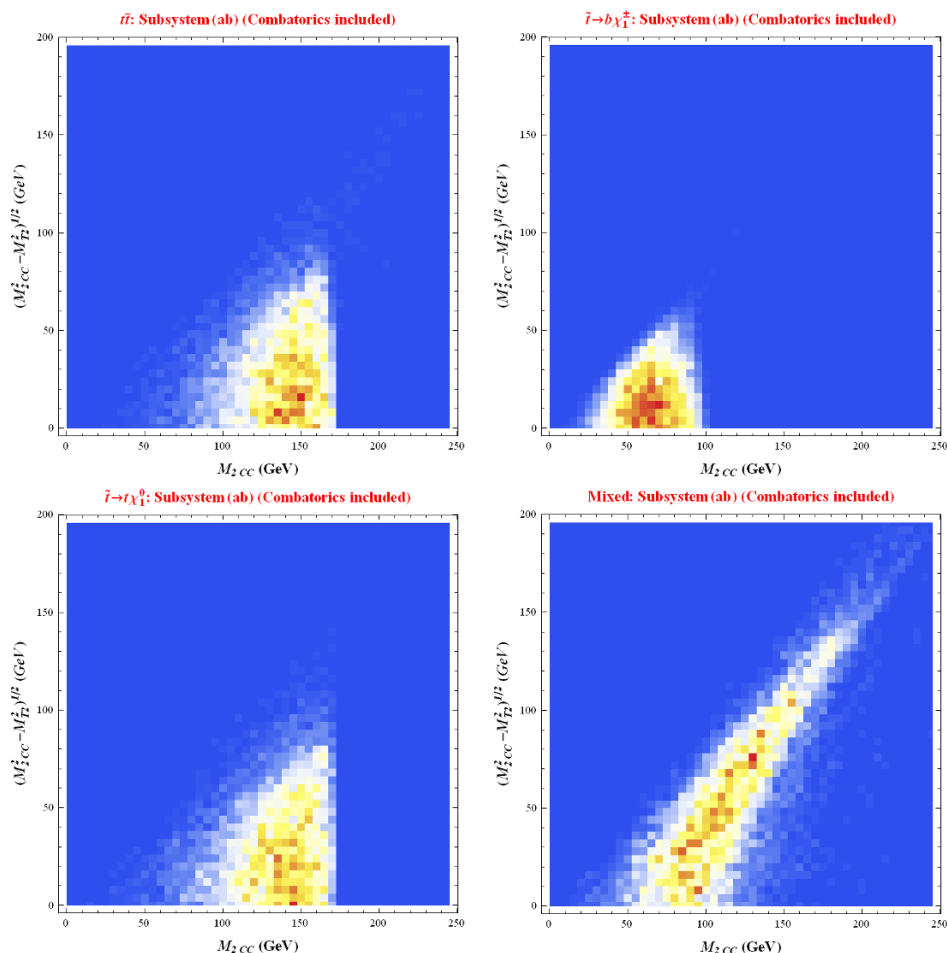
Figure 25. The same as figure 24, but including combinatoric effects: each variable M_{T2} and M_{2CC} is separately calculated with the b-ℓ pairing which gives the lower value for the corresponding variable.

the true momenta of the invisible particles in the event, they do provide an useful ansatz and can be used to calculate various $3+1$-dimensional kinematic quantities of interest [87]. (See also the MAOS method [109, 110].) In particular, we can compute the masses of the parent particles and the relative particles in the event and test whether the constraints (2.4) and (2.7) are satisfied or not. However, there is one technical complication: the function which is being minimized in order to compute M_{2XX}, sometimes has a flat direction and does not lead to a unique ansatz for the invisible momenta [87]. In order to avoid this problem, here we prefer to use the variable, M_{CX}, where the parent constraint (2.4) is already applied. Thus, we will be comparing the masses of the relative particles instead. In analogy to (6.1), we therefore define

$$\Delta M_R(S; \tilde{m}) \equiv \sqrt{|M_{R_1}^2(S; \tilde{m}) - M_{R_2}^2(S; \tilde{m})|}. \tag{6.2}$$

Since they both measure the same effect, namely, the impact of the relative constraint (2.7), we expect the two variables ΔM and ΔM_R to be correlated. This is illustrated in figure 27,
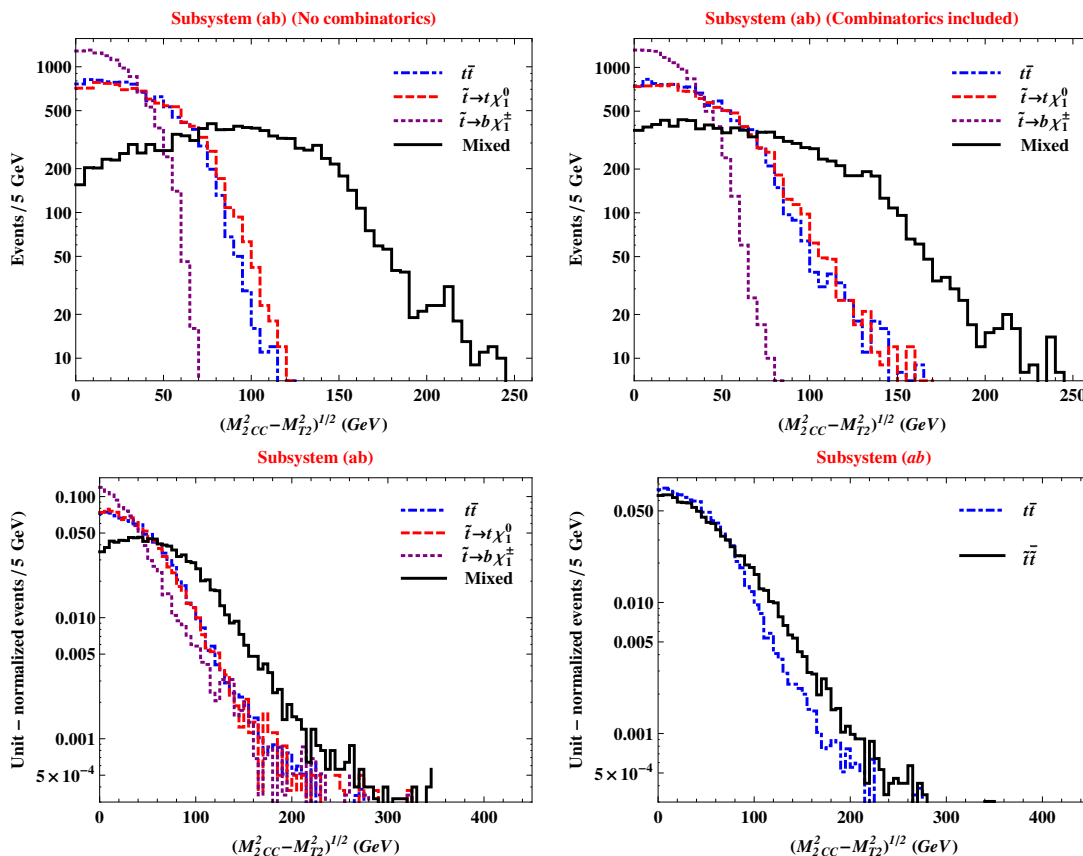
Figure 26. Unit-normalized distributions of the $\Delta M(ab)$ variable for signal and background events, with the same color coding scheme used in earlier figures. The top row shows parton level results before any selection cuts, while the bottom row includes detector simulation and selection cuts. The upper right (upper left) panel does (does not) account for the two-fold combinatorial ambiguity.

where we compare $\Delta M(ab)$ and $\Delta M_R(ab)$ for background events (left panel) and signal events with the mixed event topology of figure 2(d) (right panel). The correlation is very evident and suggests that ΔM_R can be used in place of ΔM. The advantage of using ΔM_R is convenience: in order to compute it, one needs to perform a single minimization (that of the variable M_{2CX}), while to construct ΔM, one needs to minimize twice: once for M_{T2} (or, equivalently, M_{2XX}) and then once for M_{2CC}. We have also noticed that our numerical minimization code finds the global minimum of M_{2CX} more reliably than it finds the minimum of the doubly constrained variable M_{2CC}.

7 Conclusions and outlook

The search for "top partners," like top squarks in SUSY, will be a key component of the LHC research program in the next run of the LHC. This is due to several reasons. First, particles which behave like top partners are theoretically well-motivated since they are ubiquitous in models that try to address the hierarchy problem. Second, the experimental limits on third generation partners are generally weaker, leaving room for improvement in
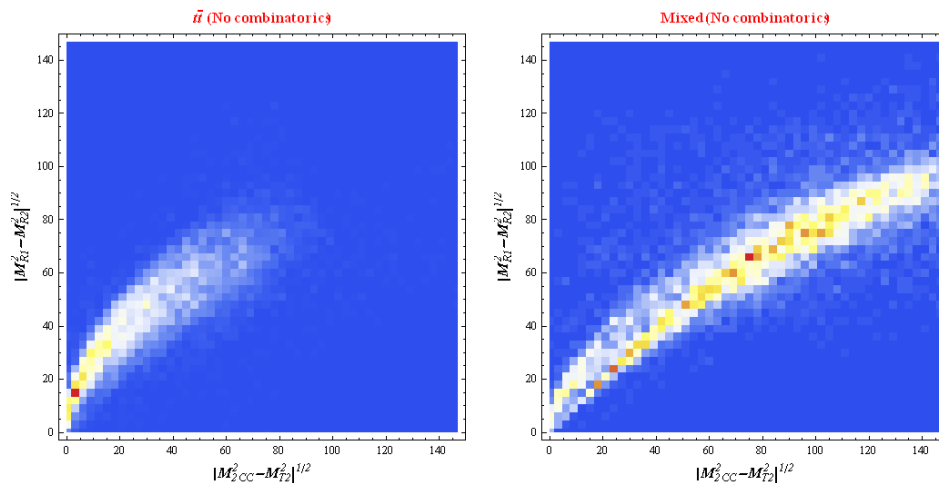
Figure 27. The correlation between the parent mass difference ΔM_R defined in (6.1) and the relative mass difference ΔM defined in (6.2) for background events (left) and signal events with the mixed event topology of figure 2(d) (right).

the next run. Third, the signatures of top partner production typically resemble those of SM top production, a process which will continue to be under close scrutiny because of the intrinsic interest in the top in its own right.

The main goal of this paper was to tackle certain *difficult* cases for stop discovery and propose new ideas for improving the experimental sensitivity in the next LHC run. We considered stop signatures which led to an *identical* final state as the main irreducible top background. Of special interest to us were corners of parameter space which would evade easy detection by normal means, either due to small mass splittings, which lead to soft jets and leptons, or because the new physics signature involves real SM top quarks. Thus we considered the two decay topologies of figure 1, which led to the three types of signal events depicted in figure 2(b-d).

Given that the signal and background are so similar, discrimination is only possible if we take full advantage of subtle kinematic differences. This is why we focused on the recently proposed class of on-shell constrained variables (M_{2XX}, M_{2CX}, M_{2XC}, and M_{2CC}) [86, 87], which can be suitably defined with the background event topology of figure 3 in mind (see appendix A). These variables have several useful properties which can be used for isolating the signal over the background:

- *Existence of upper kinematic endpoints.* While the background events obey the bounds (2.13)–(2.15), signal events may violate those bounds, depending on the new physics mass spectrum. Thus, by employing suitable high pass cuts on those variables, one can remove the majority of the background, leaving some fraction of the signal. In section 3.1, we analyzed the relevant mass parameter space and classified the regions where given kinematic endpoints for signal events exceed those for the background. The "easy" regions, where the signal endpoints are significantly above the background endpoints, should be the first targets in the next LHC runs.
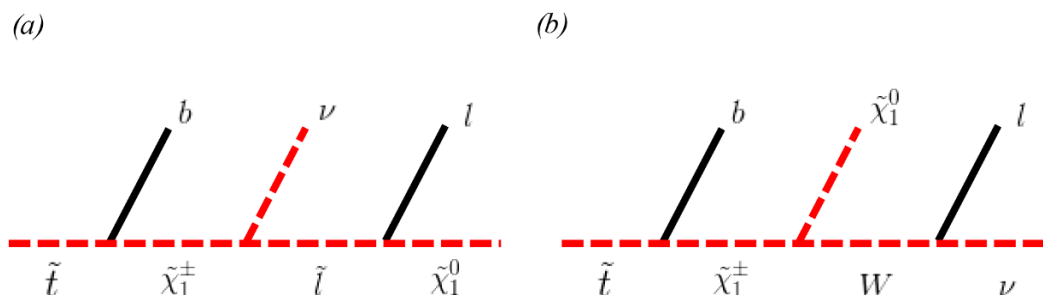
Figure 28. Two other possible decay topologies leading to the same final state as in figure 1.

- *Endpoint violation in the case of the "wrong" event topology.* The on-shell kinematic variables were defined with a specific background event topology in mind. If the signal events have a different event topology, either because they are asymmetric (e.g., the mixed event topology of figure 2(d)), or because they contain more invisible particles (as in the case of pure Topology 2 in figure 2(c)), they may again violate the background endpoints, see figures 13 and 18. For concreteness, in this paper we only considered the two specific event topologies from figure 1, but in realistic models, there exist other well-motivated event topologies which would lead to the same final state. (A couple of such examples are shown in figure 28.) The multitude of possible stop decay modes increases the likelihood that the signal will include asymmetric events, which may manifest themselves through violations of the expected background endpoints.

- *The existence of the hierarchy* (2.16) *between the various $M_{2\sqcup\sqcup}$ variables.* We showed that the hierarchy is relatively mild in the case of symmetric events like the $t\bar{t}$ background and gets stronger as the events become more asymmetric (as in the mixed topology of figure 2(d)). This observation allows us to also target signal events which are *below* the background kinematic endpoints. We believe that the related variables ΔM and ΔM_R defined in (6.1) and (6.2) respectively, will be a useful addition to the experimenter's arsenal of tools for new physics searches in missing energy events.

In spite of the advances proposed here, these searches remain extremely challenging. Detector effects, jet combinatorics issues due to ISR and FSR, and b-jet misidentification contribute to the degradation of the parton level significance.[11] Nevertheless, we believe that the techniques presented here will prove useful in searches for top partners at the LHC.

In this paper, we have employed a simplified model approach as shown in figure 2 in order to best make contact with experimental efforts. Of course, when interpreting such simplified model experimental limits or discoveries in terms of some complete theory, one must compute both signal [112–114] and background [115–118] production cross-sections and the relevant branching ratios [119] to a high degree of precision.

The on-shell constrained variables are suitable generalizations of the stransverse mass variable, M_{T2}, which is being used extensively in experimental searches, and for which

---

[11]For a more complete discussion, see [111].

several public codes exist. In contrast, there is no public code which allows the computation of the M_2 variables. We are developing such a code for public release in the near future to facilitate the wider use of M_2 variables [120].

A The complete set of M_2 variables for the $t\bar{t}$ event topology

In this appendix, we collect the specific definitions of the fifteen M_2 variables used in this paper. We consider the three subsystems in figure 3 as applied to the $t\bar{t}$ background events of figure 2(a). We write the equations in terms of the measured 4-momenta of the b and $\bar{b}$ quarks, p_b and $p_{\bar{b}}$, and the measured 4-momenta of the lepton and antilepton, $p_{\ell-}$ and $p_{\ell+}$. The invisible neutrino 4-momenta will be denoted by q_1 and q_2, where we take "1" to refer to the decay chain initiated by a top quark and "2" to refer to the decay chain initiated by an anti-top. In each subsystem, the test mass $\tilde{m}$ is taken to be the corresponding true daughter mass.

In the (ab) subsystem the daughter particles are the two neutrinos, with mass $\tilde{m} = 0$. The definitions (2.8)–(2.12) imply

$$M_{2CC}^2(ab; \tilde{m} = 0) \equiv \min_{\substack{\vec{q}_1, \vec{q}_2 \\ q_1^2 = q_2^2 = \tilde{m}^2 = 0 \\ \vec{q}_{1T} + \vec{q}_{2T} = \vec{\not{P}}_T \\ (p_b + p_{\ell+} + q_1)^2 = (p_{\bar{b}} + p_{\ell-} + q_2)^2 \\ (p_{\ell+} + q_1)^2 = (p_{\ell-} + q_2)^2}} \left\{ (p_b + p_{\ell+} + q_1)^2 \right\}, \tag{A.1}$$

$$M_{2CX}^2(ab; \tilde{m} = 0) \equiv \min_{\substack{\vec{q}_1, \vec{q}_2 \\ q_1^2 = q_2^2 = \tilde{m}^2 = 0 \\ \vec{q}_{1T} + \vec{q}_{2T} = \vec{\not{P}}_T \\ (p_b + p_{\ell+} + q_1)^2 = (p_{\bar{b}} + p_{\ell-} + q_2)^2}} \left\{ (p_b + p_{\ell+} + q_1)^2 \right\}, \tag{A.2}$$

$$M_{2XC}^2(ab; \tilde{m} = 0) \equiv \min_{\substack{\vec{q}_1, \vec{q}_2 \\ q_1^2 = q_2^2 = \tilde{m}^2 = 0 \\ \vec{q}_{1T} + \vec{q}_{2T} = \vec{\not{P}}_T \\ (p_{\ell+} + q_1)^2 = (p_{\ell-} + q_2)^2}} \left\{ \max \left[(p_b + p_{\ell+} + q_1)^2, (p_{\bar{b}} + p_{\ell-} + q_2)^2 \right] \right\}, \tag{A.3}$$

$$M_{2XX}^2(ab; \tilde{m} = 0) \equiv \min_{\substack{\vec{q}_1, \vec{q}_2 \\ q_1^2 = q_2^2 = \tilde{m}^2 = 0 \\ \vec{q}_{1T} + \vec{q}_{2T} = \vec{\not{P}}_T}} \left\{ \max \left[(p_b + p_{\ell+} + q_1)^2, (p_{\bar{b}} + p_{\ell-} + q_2)^2 \right] \right\}, \tag{A.4}$$

$$M_{T2}^2(ab; \tilde{m} = 0) \equiv \min_{\substack{\vec{q}_{1T}, \vec{q}_{2T} \\ \vec{q}_{1T} + \vec{q}_{2T} = \vec{\not{P}}_T}} \left\{ \max \left[M_{Tt}^2(\vec{q}_{1T}, \tilde{m} = 0), M_{T\bar{t}}^2(\vec{q}_{2T}, \tilde{m} = 0) \right] \right\}. \tag{A.5}$$

In the last equation M_{Tt} ($M_{T\bar{t}}$) is the transverse mass of the hypothesized top quark (anti-top quark):

$$M_{Tt}^2(\vec{q}_{1T}, \tilde{m}) \equiv (E_{Tb} + E_{T\ell+} + E_{T1})^2 - (\vec{p}_{Tb} + \vec{p}_{T\ell+} + \vec{q}_{1T})^2, \tag{A.6}$$

$$M_{T\bar{t}}^2(\vec{q}_{2T}, \tilde{m}) \equiv (E_{T\bar{b}} + E_{T\ell-} + E_{T2})^2 - (\vec{p}_{T\bar{b}} + \vec{p}_{T\ell-} + \vec{q}_{2T})^2, \tag{A.7}$$

with the transverse energies defined as usual, e.g. $E_{Ti} = \sqrt{\tilde{m}^2 + \vec{q}_{Ti}^2}$.

In the (b) subsystem the daughter particles are again the massless neutrinos, but this time we minimize the masses of the hypothesized $W^\pm$ particles:

$$M^2_{2CC}(b; \tilde{m} = 0) \equiv \min_{\substack{\vec{q}_1, \vec{q}_2 \\ q_1^2 = q_2^2 = \tilde{m}^2 = 0 \\ \vec{q}_{1T} + \vec{q}_{2T} = \vec{\rlap{/}{P}}_T \\ (p_b + p_{\ell^+} + q_1)^2 = (p_{\bar{b}} + p_{\ell^-} + q_2)^2 \\ (p_{\ell^+} + q_1)^2 = (p_{\ell^-} + q_2)^2}} \left\{ (p_{\ell^+} + q_1)^2 \right\}, \tag{A.8}$$

$$M^2_{2CX}(b; \tilde{m} = 0) \equiv \min_{\substack{\vec{q}_1, \vec{q}_2 \\ q_1^2 = q_2^2 = \tilde{m}^2 = 0 \\ \vec{q}_{1T} + \vec{q}_{2T} = \vec{\rlap{/}{P}}_T \\ (p_{\ell^+} + q_1)^2 = (p_{\ell^-} + q_2)^2}} \left\{ (p_{\ell^+} + q_1)^2 \right\}, \tag{A.9}$$

$$M^2_{2XC}(b; \tilde{m} = 0) \equiv \min_{\substack{\vec{q}_1, \vec{q}_2 \\ q_1^2 = q_2^2 = \tilde{m}^2 = 0 \\ \vec{q}_{1T} + \vec{q}_{2T} = \vec{\rlap{/}{P}}_T \\ (p_b + p_{\ell^+} + q_1)^2 = (p_{\bar{b}} + p_{\ell^-} + q_2)^2}} \left\{ \max \left[(p_{\ell^+} + q_1)^2, (p_{\ell^-} + q_2)^2 \right] \right\}, \tag{A.10}$$

$$M^2_{2XX}(b; \tilde{m} = 0) \equiv \min_{\substack{\vec{q}_1, \vec{q}_2 \\ q_1^2 = q_2^2 = \tilde{m}^2 = 0 \\ \vec{q}_{1T} + \vec{q}_{2T} = \vec{\rlap{/}{P}}_T}} \left\{ \max \left[(p_{\ell^+} + q_1)^2, (p_{\ell^-} + q_2)^2 \right] \right\}, \tag{A.11}$$

$$M^2_{T2}(b; \tilde{m} = 0) \equiv \min_{\substack{\vec{q}_{1T}, \vec{q}_{2T} \\ \vec{q}_{1T} + \vec{q}_{2T} = \vec{\rlap{/}{P}}_T}} \left\{ \max \left[M^2_{TW^+}(\vec{q}_{1T}, \tilde{m} = 0), M^2_{TW^-}(\vec{q}_{2T}, \tilde{m} = 0) \right] \right\}, \tag{A.12}$$

with

$$M^2_{TW^+}(\vec{q}_{1T}, \tilde{m}) \equiv (E_{T\ell^+} + E_{T1})^2 - (\vec{p}_{T\ell^+} + \vec{q}_{1T})^2, \tag{A.13}$$

$$M^2_{TW^-}(\vec{q}_{2T}, \tilde{m}) \equiv (E_{T\ell^-} + E_{T2})^2 - (\vec{p}_{T\ell^-} + \vec{q}_{2T})^2. \tag{A.14}$$

Finally, consider the (a) subsystem, in which the the parents are the top quarks, while the daughters are the $W^\pm$ bosons, with masses $\tilde{m} = m_W$. Denoting now the 4-momenta of the two hypothesized $W^\pm$ bosons with q_{W^+} and q_{W^-}, we have

$$M^2_{2CC}(a; \tilde{m} = m_W) \equiv \min_{\substack{\vec{q}_{W^+}, \vec{q}_{W^-} \\ q_{W^+}^2 = q_{W^-}^2 = \tilde{m}^2 = m_W^2 \\ \vec{q}_{TW^+} + \vec{q}_{TW^-} = \vec{\rlap{/}{P}}_T + \vec{p}_{T\ell^+} + \vec{p}_{T\ell^-} \\ (p_b + q_{W^+})^2 = (p_{\bar{b}} + q_{W^-})^2 \\ (q_{W^+} - p_{\ell^+})^2 = (q_{W^-} - p_{\ell^-})^2}} \left\{ (p_b + q_{W^+})^2 \right\}, \tag{A.15}$$

$$M^2_{2CX}(a; \tilde{m} = m_W) \equiv \min_{\substack{\vec{q}_{W^+}, \vec{q}_{W^-} \\ q_{W^+}^2 = q_{W^-}^2 = \tilde{m}^2 = m_W^2 \\ \vec{q}_{TW^+} + \vec{q}_{TW^-} = \vec{\rlap{/}{P}}_T + \vec{p}_{T\ell^+} + \vec{p}_{T\ell^-} \\ (p_b + q_{W^+})^2 = (p_{\bar{b}} + q_{W^-})^2}} \left\{ (p_b + q_{W^+})^2 \right\}, \tag{A.16}$$

$$M^2_{2XC}(a; \tilde{m} = m_W) \equiv \min_{\substack{\vec{q}_{W^+}, \vec{q}_{W^-} \\ q_{W^+}^2 = q_{W^-}^2 = \tilde{m}^2 = m_W^2 \\ \vec{q}_{TW^+} + \vec{q}_{TW^-} = \vec{\rlap{/}{P}}_T + \vec{p}_{T\ell^+} + \vec{p}_{T\ell^-} \\ (q_{W^+} - p_{\ell^+})^2 = (q_{W^-} - p_{\ell^-})^2}} \left\{ \max \left[(p_b + q_{W^+})^2, (p_{\bar{b}} + q_{W^-})^2 \right] \right\}, \tag{A.17}$$

$$M^2_{2XX}(a; \tilde{m} = m_W) \equiv \min_{\substack{\vec{q}_{W^+}, \vec{q}_{W^-} \\ q_{W^+}^2 = q_{W^-}^2 = \tilde{m}^2 = m_W^2 \\ \vec{q}_{TW^+} + \vec{q}_{TW^-} = \vec{\rlap{/}{P}}_T + \vec{p}_{T\ell^+} + \vec{p}_{T\ell^-}}} \left\{ \max \left[(p_b + q_{W^+})^2, (p_{\bar{b}} + q_{W^-})^2 \right] \right\}, \tag{A.18}$$

$$M_{T2}^2(a; \tilde{m} = m_W) \equiv \min_{\substack{\vec{q}_{W+}, \vec{q}_{W-} \\ \vec{q}_{TW+} + \vec{q}_{TW-} = \vec{\not{p}}_T + \vec{p}_{T\ell+} + \vec{p}_{T\ell-}}} \left\{ \max \left[M_{Tt}^2(\vec{q}_{TW+}, m_W), \ M_{T\bar{t}}^2(\vec{q}_{TW-}, m_W) \right] \right\}, \quad \text{(A.19)}$$

where now the top quark transverse masses (A.6)–(A.7) are rewritten in terms of the $W^\pm$ boson momenta, q_{W+} and q_{W-}, as

$$M_{Tt}^2(\vec{q}_{TW+}, \tilde{m} = m_W) \equiv (E_{Tb} + E_{TW+})^2 - (\vec{p}_{Tb} + \vec{q}_{TW+})^2, \quad \text{(A.20)}$$

$$M_{T\bar{t}}^2(\vec{q}_{TW-}, \tilde{m} = m_W) \equiv (E_{T\bar{b}} + E_{TW-})^2 - (\vec{p}_{T\bar{b}} + \vec{q}_{TW-})^2, \quad \text{(A.21)}$$

with $E_{TW^\pm} = \sqrt{m_W^2 + \vec{q}_{TW^\pm}^2}$.

Acknowledgments

References

[1] S.P. Martin, *A supersymmetry primer*, *Adv. Ser. Direct. High Energy Phys.* **21** (2010) 1 [hep-ph/9709356] [INSPIRE].

[2] ATLAS collaboration, *Observation of a new particle in the search for the Standard Model Higgs boson with the ATLAS detector at the LHC*, *Phys. Lett.* **B 716** (2012) 1 [arXiv:1207.7214] [INSPIRE].

[3] CMS collaboration, *Observation of a new boson at a mass of 125 GeV with the CMS experiment at the LHC*, *Phys. Lett.* **B 716** (2012) 30 [arXiv:1207.7235] [INSPIRE].

[4] ATLAS collaboration, *Search for new phenomena in final states with large jet multiplicities and missing transverse momentum at $\sqrt{s} = 8$ TeV proton-proton collisions using the ATLAS experiment*, *JHEP* **10** (2013) 130 [arXiv:1308.1841] [INSPIRE].

[5] ATLAS collaboration, *Search for supersymmetry at $\sqrt{s} = 8$ TeV in final states with jets and two same-sign leptons or three leptons with the ATLAS detector*, *JHEP* **06** (2014) 035 [arXiv:1404.2500] [INSPIRE].

[6] ATLAS collaboration, *Search for squarks and gluinos with the ATLAS detector in final states with jets and missing transverse momentum using $\sqrt{s} = 8$ TeV proton-proton collision data*, *JHEP* **09** (2014) 176 [arXiv:1405.7875] [INSPIRE].

[7] ATLAS collaboration, *Search for direct pair production of the top squark in all-hadronic final states in proton-proton collisions at $\sqrt{s} = 8\,TeV$ with the ATLAS detector*, *JHEP* **09** (2014) 015 [arXiv:1406.1122] [INSPIRE].

[8] CMS collaboration, *Search for gluino mediated bottom- and top-squark production in multijet final states in pp collisions at 8 TeV*, *Phys. Lett.* **B 725** (2013) 243 [arXiv:1305.2390] [INSPIRE].

[9] CMS collaboration, *Search for new physics in events with same-sign dileptons and jets in pp collisions at $\sqrt{s} = 8\,TeV$*, *JHEP* **01** (2014) 163 [arXiv:1311.6736] [INSPIRE].

[10] CMS collaboration, *Search for new physics in the multijet and missing transverse momentum final state in proton-proton collisions at $\sqrt{s} = 8\,TeV$*, *JHEP* **06** (2014) 055 [arXiv:1402.4770] [INSPIRE].

[11] N. Craig, *The State of Supersymmetry after Run I of the LHC*, arXiv:1309.0528 [INSPIRE].

[12] G. Altarelli and R. Ruckl, *Searching for a Scalar Top at the CERN $p\bar{p}$ Collider*, *Phys. Lett.* **B 144** (1984) 126 [INSPIRE].

[13] I.I.Y. Bigi and S. Rudaz, *Search for scalar superpartners of the top quark*, *Phys. Lett.* **B 153** (1985) 335 [INSPIRE].

[14] K.-i. Hikasa and M. Kobayashi, *Light Scalar Top at e^+e^- Colliders*, *Phys. Rev.* **D 36** (1987) 724 [INSPIRE].

[15] H. Baer, M. Drees, R. Godbole, J.F. Gunion and X. Tata, *Phenomenology of light top squarks at the Fermilab Tevatron*, *Phys. Rev.* **D 44** (1991) 725 [INSPIRE].

[16] H. Baer, J. Sender and X. Tata, *The search for top squarks at the Fermilab Tevatron Collider*, *Phys. Rev.* **D 50** (1994) 4517 [hep-ph/9404342] [INSPIRE].

[17] J.L. Lopez, D.V. Nanopoulos and A. Zichichi, *A light stop and its consequences at the Tevatron and LEP-2*, *Mod. Phys. Lett.* **A 10** (1995) 2289 [hep-ph/9406254] [INSPIRE].

[18] C.-L. Chou and M.E. Peskin, *Scalar top quark as the next-to-lightest supersymmetric particle*, *Phys. Rev.* **D 61** (2000) 055004 [hep-ph/9909536] [INSPIRE].

[19] R. Demina, J.D. Lykken, K.T. Matchev and A. Nomerotski, *Stop and sbottom searches in Run II of the Fermilab Tevatron*, *Phys. Rev.* **D 62** (2000) 035011 [hep-ph/9910275] [INSPIRE].

[20] LEP2 SUSY Working Group, *Combined LEP stop and sbottom Results 183–208 GeV*, Note LEPSUSYWG/04-02.1 (2004).

[21] ALEPH collaboration, A. Heister et al., *Search for scalar quarks in e^+e^- collisions at $\sqrt{s}$ up to 209-GeV*, *Phys. Lett.* **B 537** (2002) 5 [hep-ex/0204036] [INSPIRE].

[22] DELPHI collaboration, J. Abdallah et al., *Searches for supersymmetric particles in e^+e^- collisions up to 208-GeV and interpretation of the results within the MSSM*, *Eur. Phys. J.* **C 31** (2003) 421 [hep-ex/0311019] [INSPIRE].

[23] L3 collaboration, P. Achard et al., *Search for scalar leptons and scalar quarks at LEP*, *Phys. Lett.* **B 580** (2004) 37 [hep-ex/0310007] [INSPIRE].

[24] OPAL collaboration, G. Abbiendi et al., *Search for scalar top and scalar bottom quarks at LEP*, *Phys. Lett.* **B 545** (2002) 272 [hep-ex/0209026] [INSPIRE].

[25] CDF, D0 collaborations, M. Jaffre, *SUSY searches at the Tevatron*, *EPJ Web Conf.* **28** (2012) 09006 [arXiv:1202.0712] [INSPIRE].

[26] CDF collaboration, T. Aaltonen et al., *Search for the supersymmetric partner of the top quark in $p\bar{p}$ collisions at $\sqrt{s} =$1.96 TeV*, *Phys. Rev.* **D 82** (2010) 092001 [arXiv:1009.0266] [INSPIRE].

[27] D0 collaboration, D.S. Mackin, *Search for pair production of the supersymmetric partner of the top quark in the $\tilde{t}\bar{\tilde{t}} \to b\bar{b}\,e^{\pm}\,\mu^{\mp}\,\nu\,\bar{\nu}$ decay channel at D0*, *AIP Conf. Proc.* **1200** (2010) 271 [INSPIRE].

[28] ATLAS collaboration, *Search for direct third-generation squark pair production in final states with missing transverse momentum and two b-jets in $\sqrt{s} = 8$ TeV pp collisions with the ATLAS detector*, *JHEP* **10** (2013) 189 [arXiv:1308.2631] [INSPIRE].

[29] ATLAS collaboration, *Search for direct top-squark pair production in final states with two leptons in pp collisions at $\sqrt{s} = 8$ TeV with the ATLAS detector*, *JHEP* **06** (2014) 124 [arXiv:1403.4853] [INSPIRE].

[30] ATLAS collaboration, *Search for direct top squark pair production in events with a Z boson, b-jets and missing transverse momentum in $\sqrt{s} = 8$ TeV pp collisions with the ATLAS detector*, *Eur. Phys. J.* **C 74** (2014) 2883 [arXiv:1403.5222] [INSPIRE].

[31] ATLAS collaboration, *Measurement of the $t\bar{t}$ production cross-section using $e\mu$ events with b-tagged jets in pp collisions at $\sqrt{s} = 7$ and 8 TeV with the ATLAS detector*, *Eur. Phys. J.* **C 74** (2014) 3109 [arXiv:1406.5375] [INSPIRE].

[32] ATLAS collaboration, *Search for top squark pair production in final states with one isolated lepton, jets and missing transverse momentum in $\sqrt{s} = 8$ TeV pp collisions with the ATLAS detector*, *JHEP* **11** (2014) 118 [arXiv:1407.0583] [INSPIRE].

[33] ATLAS collaboration, *Search for strong production of supersymmetric particles in final states with missing transverse momentum and at least three b-jets at $\sqrt{s} = 8$ TeV proton-proton collisions with the ATLAS detector*, *JHEP* **1410** (2014) 24 [arXiv:1407.0600] [INSPIRE].

[34] ATLAS collaboration, *Search for pair-produced third-generation squarks decaying via charm quarks or in compressed supersymmetric scenarios in pp collisions at $\sqrt{s} = 8$ TeV with the ATLAS detector*, *Phys. Rev.* **D 90** (2014) 052008 [arXiv:1407.0608] [INSPIRE].

[35] CMS collaboration, *Search for new physics in events with same-sign dileptons and b jets in pp collisions at $\sqrt{s} = 8$ TeV*, *JHEP* **03** (2013) 037 [arXiv:1212.6194] [INSPIRE].

[36] CMS collaboration, *Search for supersymmetry in hadronic final states with missing transverse energy using the variables α_T and b-quark multiplicity in pp collisions at $\sqrt{s} = 8$ TeV*, *Eur. Phys. J.* **C 73** (2013) 2568 [arXiv:1303.2985] [INSPIRE].

[37] CMS collaboration, *Search for top squarks in R-parity-violating supersymmetry using three or more leptons and b-tagged jets*, *Phys. Rev. Lett.* **111** (2013) 221801 [arXiv:1306.6643] [INSPIRE].

[38] CMS collaboration, *Search for top-squark pair production in the single-lepton final state in pp collisions at $\sqrt{s} = 8$ TeV*, *Eur. Phys. J.* **C 73** (2013) 2677 [arXiv:1308.1586] [INSPIRE].

[39] CMS collaboration, *Search for supersymmetry in pp collisions at $\sqrt{s} = 8$ TeV in events with a single lepton, large jet multiplicity and multiple b jets*, *Phys. Lett.* **B 733** (2014) 328 [arXiv:1311.4937] [INSPIRE].

[40] CMS collaboration, *Search for top squark and higgsino production using diphoton Higgs boson decays*, *Phys. Rev. Lett.* **112** (2014) 161802 [arXiv:1312.3310] [INSPIRE].

[41] CMS collaboration, *Search for top-squark pairs decaying into Higgs or Z bosons in pp collisions at $\sqrt{s} = 8\,TeV$*, *Phys. Lett.* **B 736** (2014) 371 [arXiv:1405.3886] [INSPIRE].

[42] J.L. Feng, C.F. Kolda and N. Polonsky, *Solving the supersymmetric flavor problem with radiatively generated mass hierarchies*, *Nucl. Phys.* **B 546** (1999) 3 [hep-ph/9810500] [INSPIRE].

[43] S. Dimopoulos and G.F. Giudice, *Naturalness constraints in supersymmetric theories with nonuniversal soft terms*, *Phys. Lett.* **B 357** (1995) 573 [hep-ph/9507282] [INSPIRE].

[44] A. Pomarol and D. Tommasini, *Horizontal symmetries for the supersymmetric flavor problem*, *Nucl. Phys.* **B 466** (1996) 3 [hep-ph/9507462] [INSPIRE].

[45] A.G. Cohen, D.B. Kaplan and A.E. Nelson, *The more minimal supersymmetric standard model*, *Phys. Lett.* **B 388** (1996) 588 [hep-ph/9607394] [INSPIRE].

[46] M. Perelstein and C. Spethmann, *A collider signature of the supersymmetric golden region*, *JHEP* **04** (2007) 070 [hep-ph/0702038] [INSPIRE].

[47] K. Kong, H.-S. Lee and M. Park, *Dark decay of the top quark*, *Phys. Rev.* **D 89** (2014) 074007 [arXiv:1401.5020] [INSPIRE].

[48] T. Han, R. Mahbubani, D.G.E. Walker and L.-T. Wang, *Top Quark Pair plus Large Missing Energy at the LHC*, *JHEP* **05** (2009) 117 [arXiv:0803.3820] [INSPIRE].

[49] M. Carena, A. Freitas and C.E.M. Wagner, *Light Stop Searches at the LHC in Events with One Hard Photon or Jet and Missing Energy*, *JHEP* **10** (2008) 109 [arXiv:0808.2298] [INSPIRE].

[50] M. Perelstein and A. Weiler, *Polarized Tops from Stop Decays at the LHC*, *JHEP* **03** (2009) 141 [arXiv:0811.1024] [INSPIRE].

[51] T. Plehn, M. Spannowsky, M. Takeuchi and D. Zerwas, *Stop Reconstruction with Tagged Tops*, *JHEP* **10** (2010) 078 [arXiv:1006.2833] [INSPIRE].

[52] S. Bornhauser, M. Drees, S. Grab and J.S. Kim, *Light Stop Searches at the LHC in Events with two b-Jets and Missing Energy*, *Phys. Rev.* **D 83** (2011) 035008 [arXiv:1011.5508] [INSPIRE].

[53] X.-J. Bi, Q.-S. Yan and P.-F. Yin, *Probing Light Stop Pairs at the LHC*, *Phys. Rev.* **D 85** (2012) 035005 [arXiv:1111.2250] [INSPIRE].

[54] B. He, T. Li and Q. Shafi, *Impact of LHC Searches on NLSP Top Squark and Gluino Mass*, *JHEP* **05** (2012) 148 [arXiv:1112.4461] [INSPIRE].

[55] M. Drees, M. Hanussek and J.S. Kim, *Light Stop Searches at the LHC with Monojet Events*, *Phys. Rev.* **D 86** (2012) 035024 [arXiv:1201.5714] [INSPIRE].

[56] Y. Bai, H.-C. Cheng, J. Gallicchio and J. Gu, *Stop the Top Background of the Stop Search*, *JHEP* **07** (2012) 110 [arXiv:1203.4813] [INSPIRE].

[57] T. Plehn, M. Spannowsky and M. Takeuchi, *Stop searches in 2012*, *JHEP* **08** (2012) 091 [arXiv:1205.2696] [INSPIRE].

[58] D.S.M. Alves, M.R. Buckley, P.J. Fox, J.D. Lykken and C.-T. Yu, *Stops and $\not{E}_T$: The shape of things to come*, *Phys. Rev.* **D 87** (2013) 035016 [arXiv:1205.5805] [INSPIRE].

[59] Z. Han, A. Katz, D. Krohn and M. Reece, *(Light) Stop Signs*, *JHEP* **08** (2012) 083 [arXiv:1205.5808] [INSPIRE].

[60] D.E. Kaplan, K. Rehermann and D. Stolarski, *Searching for Direct Stop Production in Hadronic Top Data at the LHC*, *JHEP* **07** (2012) 119 [arXiv:1205.5816] [InSPIRE].

[61] E.L. Berger, Q.-H. Cao, J.-H. Yu and H. Zhang, *Measuring Top Quark Polarization in Top Pair plus Missing Energy Events*, *Phys. Rev. Lett.* **109** (2012) 152004 [arXiv:1207.1101] [InSPIRE].

[62] K. Ghosh, K. Huitu, J. Laamanen, L. Leinonen and J. Laamanen, *Top Quark Jets as a Probe of the Constrained Minimal Supersymmetric Standard Model with a Degenerate Top Squark and Lightest Supersymmetric Particle*, *Phys. Rev. Lett.* **110** (2013) 141801 [arXiv:1207.2429] [InSPIRE].

[63] C.-Y. Chen, A. Freitas, T. Han and K.S.M. Lee, *New Physics from the Top at the LHC*, *JHEP* **11** (2012) 124 [arXiv:1207.4794] [InSPIRE].

[64] C. Kilic and B. Tweedie, *Cornering Light Stops with Dileptonic mT2*, *JHEP* **04** (2013) 110 [arXiv:1211.6106] [InSPIRE].

[65] M.L. Graesser and J. Shelton, *Hunting Mixed Top Squark Decays*, *Phys. Rev. Lett.* **111** (2013) 121802 [arXiv:1212.4495] [InSPIRE].

[66] K. Krizka, A. Kumar and D.E. Morrissey, *Very Light Scalar Top Quarks at the LHC*, *Phys. Rev.* **D 87** (2013) 095016 [arXiv:1212.4856] [InSPIRE].

[67] A. Delgado, G.F. Giudice, G. Isidori, M. Pierini and A. Strumia, *The light stop window*, *Eur. Phys. J.* **C 73** (2013) 2370 [arXiv:1212.6847] [InSPIRE].

[68] B. Dutta, T. Kamon, N. Kolev, K. Sinha, K. Wang and S. Wu, *Top Squark Searches Using Dilepton Invariant Mass Distributions and Bino-Higgsino Dark Matter at the LHC*, *Phys. Rev.* **D 87** (2013) 095007 [arXiv:1302.3231] [InSPIRE].

[69] M.R. Buckley, T. Plehn and M. Takeuchi, *Buckets of Tops*, *JHEP* **08** (2013) 086 [arXiv:1302.6238] [InSPIRE].

[70] A. Chakraborty, D.K. Ghosh, D. Ghosh and D. Sengupta, *Stop and sbottom search using dileptonic M_{T2} variable and boosted top technique at the LHC*, *JHEP* **10** (2013) 122 [arXiv:1303.5776] [InSPIRE].

[71] I. Low, *Polarized charginos (and top quarks) in scalar top quark decays*, *Phys. Rev.* **D 88** (2013) 095018 [arXiv:1304.0491] [InSPIRE].

[72] Y. Bai, H.-C. Cheng, J. Gallicchio and J. Gu, *A toolkit of the stop search via the chargino decay*, *JHEP* **08** (2013) 085 [arXiv:1304.3148] [InSPIRE].

[73] G. Bélanger, D. Ghosh, R. Godbole, M. Guchait and D. Sengupta, *Probing the flavor violating scalar top quark signal at the LHC*, *Phys. Rev.* **D 89** (2014) 015003 [arXiv:1308.6484] [InSPIRE].

[74] B. Dutta et al., *Probing compressed top squark scenarios at the LHC at 14 TeV*, *Phys. Rev.* **D 90** (2014) 095022 [arXiv:1312.1348] [InSPIRE].

[75] M.R. Buckley, T. Plehn and M.J. Ramsey-Musolf, *Top squark with mass close to the top quark*, *Phys. Rev.* **D 90** (2014) 014046 [arXiv:1403.2726] [InSPIRE].

[76] N.G. Ortiz, J. Ferrando, D. Kar and M. Spannowsky, *Reconstructing singly produced top partners in decays to Wb*, *Phys. Rev.* **D 90** (2014) 075009 [arXiv:1403.7490] [InSPIRE].

[77] M. Czakon, A. Mitov, M. Papucci, J.T. Ruderman and A. Weiler, *Closing the stop gap*, *Phys. Rev. Lett.* **113** (2014) 201803 [arXiv:1407.1043] [InSPIRE].

[78] A. Ismail, R. Schwienhorst, J.S. Virzi and D.G.E. Walker, *Deconstructed Transverse Mass Variables*, *Phys. Rev.* **D 91** (2015) 074002 [arXiv:1409.2868] [INSPIRE].

[79] T. Eifert and B. Nachman, *Sneaky light stop*, *Phys. Lett.* **B 743** (2015) 218 [arXiv:1410.7025] [INSPIRE].

[80] A. Datta and S. Niyogi, *Entangled System of Squarks from the Third Generation at the Large Hadron Collider*, arXiv:1111.0200 [INSPIRE].

[81] K. Agashe, D. Kim, M. Toharia and D.G.E. Walker, *Distinguishing Dark Matter Stabilization Symmetries Using Multiple Kinematic Edges and Cusps*, *Phys. Rev.* **D 82** (2010) 015007 [arXiv:1003.0899] [INSPIRE].

[82] K. Agashe, D. Kim, D.G.E. Walker and L. Zhu, *Using M_{T2} to Distinguish Dark Matter Stabilization Symmetries*, *Phys. Rev.* **D 84** (2011) 055020 [arXiv:1012.4460] [INSPIRE].

[83] G.F. Giudice, B. Gripaios and R. Mahbubani, *Counting dark matter particles in LHC events*, *Phys. Rev.* **D 85** (2012) 075019 [arXiv:1108.1800] [INSPIRE].

[84] W.S. Cho, D. Kim, K.T. Matchev and M. Park, *Probing Resonance Decays to Two Visible and Multiple Invisible Particles*, *Phys. Rev. Lett.* **112** (2014) 211801 [arXiv:1206.1546] [INSPIRE].

[85] A.J. Barr et al., *Guide to transverse projections and mass-constraining variables*, *Phys. Rev.* **D 84** (2011) 095031 [arXiv:1105.2977] [INSPIRE].

[86] R. Mahbubani, K.T. Matchev and M. Park, *Re-interpreting the Oxbridge stransverse mass variable MT2 in general cases*, *JHEP* **03** (2013) 134 [arXiv:1212.1720] [INSPIRE].

[87] W.S. Cho et al., *On-shell constrained M_2 variables with applications to mass measurements and topology disambiguation*, *JHEP* **08** (2014) 070 [arXiv:1401.1449] [INSPIRE].

[88] C.G. Lester and D.J. Summers, *Measuring masses of semiinvisibly decaying particles pair produced at hadron colliders*, *Phys. Lett.* **B 463** (1999) 99 [hep-ph/9906349] [INSPIRE].

[89] A. Barr, C. Lester and P. Stephens, *m_{T2}: the truth behind the glamour*, *J. Phys.* **G 29** (2003) 2343 [hep-ph/0304226] [INSPIRE].

[90] A.J. Barr and C. Gwenlan, *The race for supersymmetry: using m_{T2} for discovery*, *Phys. Rev.* **D 80** (2009) 074007 [arXiv:0907.2713] [INSPIRE].

[91] B.C. Allanach, A.J. Barr, A. Dafinca and C. Gwenlan, *Discovery reach for generic supersymmetry at the LHC: M_{T2} versus missing transverse momentum selections for pMSSM searches*, *JHEP* **07** (2011) 104 [arXiv:1105.1024] [INSPIRE].

[92] H. Murayama, M.M. Nojiri and K. Tobioka, *Improved discovery of a nearly degenerate model: MUED using M_{T2} at the LHC*, *Phys. Rev.* **D 84** (2011) 094015 [arXiv:1107.3369] [INSPIRE].

[93] M. Burns, K. Kong, K.T. Matchev and M. Park, *Using Subsystem M_{T2} for Complete Mass Determinations in Decay Chains with Missing Energy at Hadron Colliders*, *JHEP* **03** (2009) 143 [arXiv:0810.5576] [INSPIRE].

[94] G.G. Ross and M. Serna, *Mass determination of new states at hadron colliders*, *Phys. Lett.* **B 665** (2008) 212 [arXiv:0712.0943] [INSPIRE].

[95] W.S. Cho, J.E. Kim and J.-H. Kim, *Amplification of endpoint structure for new particle mass measurement at the LHC*, *Phys. Rev.* **D 81** (2010) 095010 [arXiv:0912.2354] [INSPIRE].

[96] A.J. Barr, B. Gripaios and C.G. Lester, *Transverse masses and kinematic constraints: from the boundary to the crease*, *JHEP* **11** (2009) 096 [arXiv:0908.3779] [INSPIRE].

[97] P. Konar, K. Kong, K.T. Matchev and M. Park, *Dark Matter Particle Spectroscopy at the LHC: Generalizing M(T2) to Asymmetric Event Topologies*, *JHEP* **04** (2010) 086 [arXiv:0911.4126] [INSPIRE].

[98] W.S. Cho, K. Choi, Y.G. Kim and C.B. Park, *Measuring the top quark mass with m(T2) at the LHC*, *Phys. Rev.* **D 78** (2008) 034019 [arXiv:0804.2185] [INSPIRE].

[99] J. Smith, W.L. van Neerven and J.A.M. Vermaseren, *The Transverse Mass and Width of the W Boson*, *Phys. Rev. Lett.* **50** (1983) 1738 [INSPIRE].

[100] V.D. Barger, A.D. Martin and R.J.N. Phillips, *Perpendicular ν_e Mass From W Decay*, *Z. Phys.* **C 21** (1983) 99 [INSPIRE].

[101] W.S. Cho, K. Choi, Y.G. Kim and C.B. Park, *Gluino Stransverse Mass*, *Phys. Rev. Lett.* **100** (2008) 171801 [arXiv:0709.0288] [INSPIRE].

[102] W.S. Cho, K. Choi, Y.G. Kim and C.B. Park, *Measuring superparticle masses at hadron collider using the transverse mass kink*, *JHEP* **02** (2008) 035 [arXiv:0711.4526] [INSPIRE].

[103] P. Konar, K. Kong and K.T. Matchev, $\sqrt{\hat{s}}_{\min}$*: a global inclusive variable for determining the mass scale of new physics in events with missing energy at hadron colliders*, *JHEP* **03** (2009) 085 [arXiv:0812.1042] [INSPIRE].

[104] J. Alwall et al., *The automated computation of tree-level and next-to-leading order differential cross sections and their matching to parton shower simulations*, *JHEP* **07** (2014) 079 [arXiv:1405.0301] [INSPIRE].

[105] R.D. Ball et al., *Parton distributions with LHC data*, *Nucl. Phys.* **B 867** (2013) 244 [arXiv:1207.1303] [INSPIRE].

[106] T. Sjöstrand, S. Mrenna and P.Z. Skands, *PYTHIA 6.4 Physics and Manual*, *JHEP* **05** (2006) 026 [hep-ph/0603175] [INSPIRE].

[107] DELPHES 3 collaboration, J. de Favereau et al., *DELPHES 3, A modular framework for fast simulation of a generic collider experiment*, *JHEP* **02** (2014) 057 [arXiv:1307.6346] [INSPIRE].

[108] M. Cacciari, G.P. Salam and G. Soyez, *The Anti-k(t) jet clustering algorithm*, *JHEP* **04** (2008) 063 [arXiv:0802.1189] [INSPIRE].

[109] W.S. Cho, K. Choi, Y.G. Kim and C.B. Park, M_{T2}*-assisted on-shell reconstruction of missing momenta and its application to spin measurement at the LHC*, *Phys. Rev.* **D 79** (2009) 031701 [arXiv:0810.4853] [INSPIRE].

[110] C.B. Park, *Reconstructing the heavy resonance at hadron colliders*, *Phys. Rev.* **D 84** (2011) 096001 [arXiv:1106.6087] [INSPIRE].

[111] D. Kim, H.-S. Lee and M. Park, *Invisible dark gauge boson search in top decays using a kinematic method*, *JHEP* **03** (2015) 134 [arXiv:1411.0668] [INSPIRE].

[112] W. Beenakker, M. Krämer, T. Plehn, M. Spira and P.M. Zerwas, *Stop production at hadron colliders*, *Nucl. Phys.* **B 515** (1998) 3 [hep-ph/9710451] [INSPIRE].

[113] W. Beenakker, S. Brensing, M. Krämer, A. Kulesza, E. Laenen and I. Niessen, *Supersymmetric top and bottom squark production at hadron colliders*, *JHEP* **08** (2010) 098 [arXiv:1006.4771] [INSPIRE].

[114] W. Beenakker et al., *Squark and Gluino Hadroproduction*, *Int. J. Mod. Phys.* **A 26** (2011) 2637 [arXiv:1105.1110] [inSPIRE].

[115] M. Cacciari, M. Czakon, M. Mangano, A. Mitov and P. Nason, *Top-pair production at hadron colliders with next-to-next-to-leading logarithmic soft-gluon resummation*, *Phys. Lett.* **B 710** (2012) 612 [arXiv:1111.5869] [inSPIRE].

[116] M. Czakon and A. Mitov, *Top++: A Program for the Calculation of the Top-Pair Cross-Section at Hadron Colliders*, *Comput. Phys. Commun.* **185** (2014) 2930 [arXiv:1112.5675] [inSPIRE].

[117] M. Czakon and A. Mitov, *NNLO corrections to top-pair production at hadron colliders: the all-fermionic scattering channels*, *JHEP* **12** (2012) 054 [arXiv:1207.0236] [inSPIRE].

[118] M. Czakon and A. Mitov, *NNLO corrections to top pair production at hadron colliders: the quark-gluon reaction*, *JHEP* **01** (2013) 080 [arXiv:1210.6832] [inSPIRE].

[119] A. Djouadi, M.M. Muhlleitner and M. Spira, *Decays of supersymmetric particles: The Program SUSY-HIT (SUspect-SdecaY-Hdecay-InTerface)*, *Acta Phys. Polon.* **B 38** (2007) 635 [hep-ph/0609292] [inSPIRE].

[120] W.S. Cho et al., *A computer package for computing constrained invariant mass variables*, in preparation.